Post-extinction recovery of the Phanerozoic oceans and the rise of biodiversity hotspots

Pedro Cermeño[1,†,*], Carmen García-Comas[1,†,*], Alexandre Pohl[2,3], Simon Williams[4], Michael J. Benton[5], Chhaya Chaudhary[6], Guillaume Le Gland[1], R. Dietmar Müller[7], Andy Ridgwell[2], Sergio M. Vallina[8]

[1]Institut de Ciències del Mar, Consejo Superior de Investigaciones Científicas, Pg. Marítim de la Barceloneta 37-49, 08003 Barcelona, Spain.
[2]Department of Earth and Planetary Sciences, University of California, Riverside, Riverside, CA, USA.
[3]Biogéosciences, UMR 6282, UBFC/CNRS, Université Bourgogne Franche-Comté, 6 boulevard Gabriel, F-21000 Dijon, France.
[4]State Key Laboratory of Continental Dynamics, Department of Geology, Northwest University, Xi'an, China.
[5]School of Earth Sciences, University of Bristol, Queens Road, Bristol, BS8 1RJ UK.
[6]Alfred Wegener Institute, Helmholtz Centre for Polar and Marine Research, Germany.
[7]EarthByte Group, School of Geosciences, University of Sydney, NSW, 2006, Sydney, Australia.
[8]Instituto Español de Oceanografía, Consejo Superior de Investigaciones Científicas, Ave. Principe de Asturias 70 bis, 33212 Gijón, Spain.

[†]These authors contributed equally to this work.

*Corresponding authors: pedrocermeno@icm.csic.es
cgcomas@icm.csic.es

Abstract

The fossil record of marine invertebrates has long fueled the debate as to whether or not there are limits to global diversity in the sea[1–5]. Ecological theory states that as diversity grows and ecological niches are filled, the strengthening of biological interactions imposes limits on diversity[6,7]. However, the extent to which biological interactions have constrained the growth of diversity over evolutionary time remains an open question[1–5,8–11], largely because of the incompleteness and spatial heterogeneity of the fossil record[12–14]. Here we present a regional diversification model that reproduces the main Phanerozoic trends in the global diversity of marine invertebrates after imposing mass extinctions. We find that the dynamics of global diversity is best described by a diversification model that operates broadly within the exponential growth regime of a logistic function. A spatially resolved analysis of the diversity-to-carrying capacity ratio reveals that < 2% of the global flooded continental area throughout the Phanerozoic exhibits diversity levels approaching ecological saturation. We attribute the overall increase in global diversity during the Late Mesozoic and Cenozoic to the development of diversity hotspots under prolonged conditions of Earth system stability and maximum continental fragmentation. We call this the "diversity hotspots hypothesis", which is proposed as a non-mutually exclusive alternative to the hypothesis that the Mesozoic marine revolution led this macroevolutionary trend[15,16].

Main

The question of whether or not there is an equilibrium diversity that the biota, or portions of the biota, cannot exceed has led to decades of debate between those who think that there is a limit to the global diversity that the Earth can carry[2,3,10] (i.e., a carrying capacity or saturation level) and those who think that diversity can increase in an unlimited fashion over time or, alternatively, that the biosphere is so far from the equilibrium diversity (i.e., its carrying capacity) that we can ignore the existence of any limit[4,5,11]. This question has traditionally been addressed by examining the shape of global fossil diversity curves[3,17]. For example, the Paleozoic plateau in marine invertebrate diversity is generally taken as strong evidence for the existence of ecological limits to further diversification[3,18]. However, because diversity varies dramatically among geographic regions, and each geographic region has its own geological and environmental history, addressing this question requires simultaneously reconstructing the dynamics of regional diversity in both space and time[13,19]. If diversity dynamics were governed by diversity-dependent feedbacks on speciation and extinction rates, then regional diversity should remain stable regardless of time once carrying capacity has been reached (i.e., the logistic model). The reasoning is the same as that used to explain the logistic growth model in population dynamics in which the per capita rate of increase decreases as the population approaches its maximum size or carrying capacity. Conversely, if evolutionary rates were independent of standing diversities, then we should observe positive relationships between evolutionary time-within-regions (or time-for-speciation) and diversity; the older the habitat the longer the lineages have had to diversify and fill empty niches or explore new ones (i.e., the exponential model). The reasoning in this case is the same as that used to explain the exponential growth model in population dynamics in which the per capita rate of increase does not depend on the population size but only on the modulating effects of environmental conditions. Determining which diversification model best

describes the dynamics of regional diversity over time is key to understanding the mechanisms underlying biogeographic patterns and macroevolutionary trends. However, the fossil record is biased by uneven geographic and stratigraphic sampling effort[12,13] and variation in the rock record available for sampling[20], hindering our ability to investigate the effect of geographic variability in evolutionary time and diversification rate.

In order to overcome this limitation, we couple two alternative models of diversification – logistic and exponential – to a global model of palaeogeography and plate-motion that constrains evolutionary time-within-regions (i.e. the age of the seafloor for the deep ocean and the time underwater for the flooded continental regions). In both diversification models, the net diversification rate varies within a fixed range of values as a function of seawater temperature and food supply, which are reconstructed using a spatially explicit Palaeo-Earth system model (Methods). In the logistic model, the spatially resolved effective carrying capacities (K_{eff}) are allowed to vary within a fixed range of values (K_{min} and K_{max}) as a positive linear function of the food supply in each ocean region and time. We set relatively low K_{min} and K_{max} values (4 and 16 genera, respectively) to enforce diversity saturation, hereinafter referred to as 'saturated' logistic model. Mass extinctions are imposed by imputing negative net diversification rates to regional communities and assuming non-selective extinction. The percentage of diversity loss as well as the starting time and duration of mass extinctions are extracted from three fossil diversity curves of reference, namely Sepkoski[21], Alroy[22] and Zaffos et al[23]. Each of these curves provides alternative insights into the Phanerozoic history of marine animal diversity based on uncorrected range-through genus richness estimates[21,23] and sampling standardized estimates[22].

Reconstructing global diversity dynamics

Each of the two diversification models tested here produces a total of 82 spatially-explicit reconstructions of diversity spanning from the Cambrian (541 Ma) to the present (**Supplementary Videos 1-2**). On each of the 82 diversity distribution maps, we trace hundreds of line transects from diversity peaks to their nearest diversity troughs and integrate the total diversity in each transect by assuming a decay function in taxonomic similarity with geographic distance (Methods, **Extended Data Fig. 1**). Then, for each of the 82 time intervals, all integrated diversities along transects are re-integrated step-wise, from the transect with the greatest diversity to the transect with the lowest one, assuming the same distance-decay function applied to individual transects. The resulting global diversity estimates are plotted against the mid-point value of the corresponding time interval to generate a synthetic global diversity curve. Both the saturated logistic model and the exponential model produce relatively similar global diversity dynamics (**Fig. 1**). This is expected since the global diversity curves produced by both models were equally influenced by mass extinctions as well as long-term variations in the global area of shallow shelf seas (**Extended Data Fig. 2**), which harbour the vast majority of the diversity of marine invertebrates. However, while both models show similar diversity dynamics, the amplitudes of global diversity variations differ markedly between models depending on whether or not regional-scale diversities self-limit their increase over time (**Fig. 1**). The exponential model gives rise to conspicuous increases in global diversity from the Cambrian to Late Ordovician, Silurian to Early Devonian, Carboniferous (Early to Late Pennsylvanian), Early to Late Cretaceous, and Paleocene to present. The Permian-Triassic mass extinction event lowered global diversity to Early Palaeozoic levels, but later diversification led Late Cretaceous and Neogene faunas to exceed the Mid-Palaeozoic global diversity peak. These trends emerge consistently regardless of the mass extinctions pattern imposed, be it Sepkoski[21], Alroy[22], or Zaffos et al.[23] (**Fig. 1**). Nevertheless, it is worth noting how well the exponential model reproduces the Sepkoski ‘uncorrected’ fossil diversity curve. The logistic model also

reproduces the initial increase in diversity, from Cambrian to Late Ordovician and from Silurian to Early Devonian (**Fig. 1**). However, unlike the exponential model, in the saturated logistic model this initial upward trend is followed by a convex diversity pattern interrupted by a modest increase during the Cretaceous, which rarely exceeds the mid-Palaeozoic global diversity peak in our set of simulations.

The calibrated logistic model

The logistic model allows the spatially-resolved effective carrying capacities (K_{eff}) to vary within a fixed range of values (from K_{min} to K_{max}) as a positive linear function of food availability in each ocean region and time (Methods). All other things being equal, the higher the K_{min} and K_{max} values, the longer the evolutionary time required to reach diversity saturation. Consequently, the choice of K_{min} and K_{max} critically influences the extent to which regional biotas reach saturation. In order to calibrate the K_{min} and K_{max} parameters, we run simulations of pair-wise K_{min} and K_{max} combinations in a geometric sequence of base 2, from 2 to 256 genera, and test the effect of changing the K_{min} and K_{max} values on the concordance between the normalized diversities generated by the model and those estimated from the fossil record. Unlike other correlation coefficients, Lin's concordance correlation coefficient[24] (CCC) combines measures of both precision and accuracy to determine how far the modelled data deviate from the line of perfect concordance. We focus the analysis on the time series data between the end of one mass extinction and the beginning of the next, that is, considering those time intervals dominated by rising diversity trajectories. Lin's CCC increases with increasing K_{min} and K_{max} until reaching a plateau except for the mass extinction pattern of Sepkoski for which it continues to increase even at the highest K_{min} and K_{max} values (**Extended Data Figs. 3–5**). These results are consistently replicated using alternative values

for the parameters of the model that define the temperature- and food-dependence of the net diversification rate (**Extended Data Fig. 6,** grey lines in insets, **Extended Data Table 1**).

Then, we re-run the logistic model using the average of all K_{min} and K_{max} combinations giving a CCC greater than 0.70, hereinafter referred to as 'calibrated' logistic model. The calibrated model generates global diversity curves half way between the two end-member diversification models, the saturated logistic and the exponential (**Fig. 1**). Most of the diversity is concentrated in shallow marine environments, where high temperatures and abundant food supplies increase the rates of diversification compared to the deep sea habitats (**Fig. 2a-f**, **Extended Data Figs. 7-8**). Diversity hotspots occur in tropical shelf seas of the Early Devonian, Permian, Late Cretaceous and Cenozoic (**Fig. 2c-f**, **Supplementary Video 3**). During the Early Devonian, diversity hotspots developed on the western continental margins of Laurentia and Siberia as well as on the tropical shelves of Gondwana. The recovery of Laurentian diversity hotspots after the Late Devonian mass extinction led to the onset of Permian hotspots, which eventually disappeared during the Permian-Triassic mass extinction. Diversity hotspots became particularly prominent during the Late Cretaceous and Cenozoic in the western basins of the Tethys Ocean, the Arabian Peninsula, the Atlantic Caribbean-East Pacific and the Indo-West Pacific provinces (**Fig. 2e-f**). This temporal trend in the prominence of diversity hotspots cannot be explained by a secular increase in the maximum lifetime of shelf seas, a proxy for the maximum potential evolutionary time-within-regions. Geological data from ancient continental margins trapped within orogenic belts[25] and global tectonic reconstructions[26] (see seafloor age in **Supplementary Fig. 1**), show no evidence of an increase in the lifespan of passive continental margins or in the maximum ages of the seafloor over the Phanerozoic. Rather, we argue that the temporal proximity between the Ordovician-Silurian (Hirnantian), Late Devonian (Frasnian-Famennian), and Permian-Triassic mass extinctions, coinciding with a long-lived phase of continental coalescence and

destruction of marine shelves during the assembly of Pangaea, interrupted the full development of diversity hotspots during the Palaeozoic. By contrast, the comparatively long expanse of time that separated the mass extinctions of the end-Triassic and end-Cretaceous extended the time-for-speciation under conditions of increasing continental fragmentation, giving rise to exceptionally high-diversity regions before the Cretaceous-Paleogene mass extinction. The extraordinary diversity of Late Cretaceous hotspots ensured the continuity of relatively high diversity levels in the aftermath of the end-Cretaceous mass extinction, facilitating the subsequent development of diversity hotspots during the Cenozoic.

In order to evaluate the model's performance in reconstructing the spatial distributions of diversity, we compare the results of the calibrated logistic model for the recent (i.e., 0 Ma) with observations of marine invertebrates (crustaceans and molluscs) extracted from the Ocean Biodiversity Information System (OBIS), a global database of occurrence records of marine taxa (Methods). The regional diversity map generated by the model shows reasonable similarities to the observed diversity distributions along the continental margins (**Fig. 2g-h**). The main discrepancies between the model and the OBIS data occur in the surroundings of Australia and New Zealand, where the model underestimates diversity. Although the model accounts for coastal re-colonization during marine transgressions, it lacks long-distance dispersal, which precludes a more detailed reconstruction of the spatial structuring of diversity in such a highly interconnected ocean region. Despite some regional discrepancies, both observed and modeled diversity decline from the equator towards the poles (**Fig. 2i-j**), with most diversity concentrated in the Indo-West Pacific, the Atlantic Caribbean-East Pacific, and the Mediterranean (**Fig. 2g-h**).

Using the outputs of the calibrated logistic model, we analyse the spatial and temporal variability of the diversity-to-carrying capacity (K_{eff}) ratio. This ratio provides a quantitative

index of how far (ratios close to zero) or how close (ratios close to one) are the regional faunas from noticing the effect of diversity-dependent ecological factors (i.e. the proximity to diversity saturation). The diversity-to-K_{eff} ratio falls below 0.25 in most of the ocean and throughout the Phanerozoic (**Fig. 3a-l**, **Supplementary Video 4**), supporting the idea that the dynamics of regional diversity have been systematically operating below K_{eff} and, therefore, far from diversity saturation.

Finally, we calculate the diversity-to-K_{eff} ratio along the flooded continental regions using the combinations of K_{min} and K_{max} that resulted from simulations with different parameter values (**Extended Data Fig. 6,** grey lines in insets, **Extended Data Table 1**), and represent its frequency distributions (**Fig. 3m-o**). Most of the estimates fall within the exponential growth regime of the logistic function (i.e. diversity-to-K_{eff} ratio < 0.25). On average, less than 10% of the estimates exceed the threshold of 0.25, and only < 2% of the estimates, those associated with well-developed diversity hotspots, exceed the threshold of 0.5.

A deliberate decrease of 25% in the K_{min} and K_{max} values of the model does not significantly alter the shape of the diversity-to-K_{eff} ratio frequency distributions (**Extended Data Fig. 9**), indicating that the resulting patterns are robust. Furthermore, the relatively short time elapsed between successive Palaeozoic mass extinctions interrupted the development of diversity hotspots, preventing them from reaching saturation. In fact, by deactivating the Late Devonian mass extinction in the model, we find that the full development of diversity hotspots before the end of the Permian leads to global diversities two to three times greater than those generated by the same calibrated logistic model with all mass extinctions enabled (**Extended Data Fig. 10**).

Discussion

Our model corroborates earlier claims that Earth's environmental history[5,27,28] and the patterns of continental fragmentation and reassembly[23,29,30] have been major determinants of marine animal diversification. For example, we find that turning off plate tectonics prevents continental shelf habitats from repositioning along the latitudinal temperature gradient, causing diversity to grow disproportionately in shelf seas that lie within the tropical belt (Methods, **Supplementary Fig. 2**). The result is a rapid increase in global diversity that even mass exitinctions cannot dampen (**Supplementary Fig. 3a-c**), and only effective carrying capacities prevent diversity from running away (**Supplementary Fig. 3d-f**). A static geographic configuration also prevents diversity hotspots from disappearing at convergent plate boundaries, further limiting the model's ability to reproduce the spatial distributions of diversity and its global dynamics. Alternatively, by disabling the temperature and/or food dependence of the net diversification rate, the model produces unrealistic biogeographic distributions, such as the occurrence of diversity hotspots in high-latitudes, leaving the growth of diversity as a function of age (Methods, **Supplementary Fig. 4**).

Caveats? Sensitivity analyses (**Extended Data Fig. 11**) (this could be inserted HERE?)

Overall, we find that the temporal proximity between successive mass extinctions, along with the long-term reduction in the global area of marine shelf during the assembly of Pangea, interrupted the development of diversity hotspots throughout the Palaeozoic. In contrast, we also find evidence of regional biota approaching diversity saturation at post-Palaeozoic diversity hotspots, the development of which helps explain the increase in global diversity during the Late Mesozoic and Cenozoic. It has been hypothesized that the Mesozoic marine revolution[15,16], that is, the emergence of shell-crushing predators and the consequent ecological restructuring of marine ecosystems, was primarily responsible for the increase in global diversity over the last 150 million years. The fact that our model can reproduce such an increase in diversity without the need to invoke evolutionary innovations like the emergence of new modes of predation[15,16], defence[15,31], mobility[31] or reproduction[32], among others, raises a new hypothesis based on how Earth's environmental history and palaeogeographic evolution interacted in concert to allow the development of diversity hotspots. We call this the "diversity hotspots hypothesis", which is proposed as a non-mutually exclusive alternative to the hypothesis that evolutionary innovation and new ecospace occupation led this macroevolutionary trend.

We cannot reject the hypothesis that diversity saturation slowed down diversification in ocean regions where marine faunas i) had long development times, ii) evolved rapidly and/or iii) evolved from relatively high initial diversities. The differences between the global diversity curves resulting from the exponential model and those generated by the calibrated logistic model reveal the effect of ecological saturation on the dynamics of global diversity (**Fig. 1**). However, with the possible exception of tropical diversity hotspots, our results indicate that the diversity of marine invertebrates has remained below saturation throughout their evolutionary history, shedding light on one of the most controversial topics in evolutionary ecology[1-5,8-11]. A taxonomic diversification model operating widely within the exponential

growth regime of the logistic function implies a concave-upward relationship between the magnitude of diversity loss (x-axis) and the subsequent rebuilding time. This mode of diversification provides a plausible explanation for the observed decoupling between mass extinctions and explosive evolutionary radiations over the Phanerozoic[33]. We envision that our spatially-explicit reconstructions of diversity could shed light on other long-standing questions in (palaeo)biogeography and macroevolution and, increasing a synthetic spatially-resolved history of biodiversity through geological time, will provide a means of exploring sampling biases in the fossil record.

Methods

Palaeogeographic model

We use palaeogeographic reconstructions describing Earth's palaeotopography and palaeobathymetry for a series of time slices from 541 Ma to the present day. The reconstructions merge existing models from two published global reconstruction datasets, those of Merdith et al[34] and Scotese and Wright[35] (https://doi.org/10.5281/zenodo.5348492), which themselves are syntheses of a wealth of previous work.

For continental regions, estimates of palaeoelevation and continental flooding rely on a diverse range of geological evidence such as sedimentary depositional environments and the spatio-temporal distribution of volcanic activity. For a full description, see the recent review of Scotese[36]. Together, these data can be used to define the past locations of mountain ranges and palaeoshorelines[36]. For this part of our reconstruction, we use the compilation of Scotese and Wright[35] with updated palaeoshorelines based on depositional environment information in current fossil databases[37]. This compilation comprises 82 palaeotopography maps covering the entire Phanerozoic. It is important to note that each palaeogeographic map is a time-slice representing the concatenation of geological data over several million years[38]. Eustatic sea-level is thought to have varied by ~100 m at timescales much shorter than the duration of the time-slices throughout the Phanerozoic[39], so that the extent of continental flooding could have varied within each time-slice by an amount significant for our analysis. For this reason, and to assess the uncertainty of our results to continental palaeogeography in general, we compute additional maps of continental flooding for the analysis below in which the sea-level is raised or lowered by 100 m compared to the original paleoDEM grids of Scotese and Wright[35]. The

curves obtained differ very little from the original curves except for Zaffos et al[23] in which the Cenozoic rise in diversity is more prominent (**Extended Data Fig. 11**).

For deep ocean regions, the primary control on seafloor depth is the age of the seafloor, so reconstructing palaeobathymetry relies on constructing maps of seafloor age back in time[40]. Consequently, we rely on reconstruction models that incorporate a continuous network of plate boundaries. These models allow us to derive maps of seafloor age in deep time. For this part, we use the reconstruction of Merdith et al[34] and derive maps of seafloor age from the plate tectonic model using the method of Williams et al[41], for which source code is available at https://github.com/siwill22/agegrid-0.1. Palaeobathymetry is derived from the seafloor age maps following the steps outlined by Müller et al[40]. It is important to note that seafloor age maps for most of the Phanerozoic (i.e. pre-Pangea times) are not directly constrained by data due to recycling of oceanic crust at subduction zones. Rather, they are model predictions generated by constructing plate motions and plate boundary configurations from the geological and palaeomagnetic record of the continents. Nonetheless, the first-order trends in ocean-basin volume and mean seafloor age are consistent with independent estimates for at least the last 410 Myr[41].

The reconstructions of Merdith et al[34] and Scotese and Wright[35] differ in the precise locations of the continents through time. To resolve this discrepancy, we reverse reconstruct the Scotese and Wright[35] continental palaeoelevation model to present-day coordinates using their rotation parameters, then reconstruct them back in time using the rotations of Merdith et al[34]. Due to the differences in how the continents are divided into different tectonic units, this process leads to some gaps and overlaps in the results[42], which we resolve primarily through a combination of data interpolation and averaging. Manual adjustments are made to ensure that the flooding history remains consistent with the original palaeotopography in areas where

interpolation gives a noticeably different history of seafloor ages. The resulting palaeotopography maps are thus defined in palaeomagnetic reference frame[34] appropriate for use in Earth System models.

For the biodiversity modelling, we generate estimates of the age of the seafloor for discrete points within the oceans and flooded continents, and track these ages through the lifetime of each point. For the oceans, this is achieved using the method described by Williams et al[41] where the seafloor is represented by points incrementally generated at the mid-ocean ridges for a series of time-step 1 Myr apart, with each point tracked through subsequent time-steps based on Euler poles of rotation until either present-day is reached, or they arrive at a subduction zone and are considered destroyed.

For the continents, tracking the location of discrete points is generally simpler since most crust is conserved throughout the timespan of the reconstruction. Unlike the deep oceans (where we assume that crust is at all times submerged), we model the 'age' of the seafloor from the history of continental flooding and emergence within the palaeogeographic interpretation[35]. The continents are seeded with uniformly distributed points at the oldest timeslice (541 Ma) where they are assigned an age of zero. These points are tracked to subsequent time slices where the palaeogeography is used to determine whether the point lies within a flooded or emergent region. Points within flooded regions of continents are considered to be seafloor, and the age of this seafloor is accumulated across consecutive time slices where a given point lies within a flooded region. When a point is within an emergent region, the seafloor age is reset to zero. Following this approach, individual points within stable continents may undergo several cycles of seafloor age increasing from zero before being reset. At the continental margins formed during Pangea breakup, the age of the seafloor continuously grows from the onset of rifting. Intra-oceanic island arcs represent an

additional case, which can appear as new tectonic units with the reconstructions at various times. In these cases, we assume that the seafloor has a zero-age at the time the intra-oceanic arc first develops, then remains predominantly underwater for the rest of its lifetime. The estimated age of the seafloor of open ocean regions and the estimated time that flooded continental shelves spend underwater using the approach described in this section is shown in **Supplementary figure 1**.

Therefore, for each of the 82 palaeogeographic reconstructions, we annotate 0.5º by 0.5º grids as continental, flooded continental shelf, or oceanic for later use in model coupling and production of regional diversity maps.

Palaeo-environmental conditions: cGenie Earth System model

We use cGENIE[43], an Earth System model of intermediate complexity, to simulate palaeo-environmental conditions of seawater temperature and organic carbon export production (as a surrogate for food supply) throughout the Phanerozoic (from 541 Ma to present day).

cGENIE is based on a 3-dimensional (3D) ocean circulation model coupled to a 2D energy-moisture-balance atmospheric component and a sea-ice module. We configure the model on a 36×36 (lat, lon) equal area grid with 17 unevenly spaced vertical levels in depth, down to a maximum ocean depth of 5,900 m. The cycling of carbon and associated tracers in the ocean is based on a size-structured plankton ecosystem model with a single (phosphate) nutrient[44,45], and adopts an Arrhenius-type temperature-dependent scheme for the remineralization of organic matter exported to the ocean interior[46].

cGENIE provides a spatially resolved representation of ocean physics and biogeochemistry, which is a prerequisite for the present study to be able to reconstruct the spatial patterns of biodiversity in deep time. However, because of the computational impracticality of generating a single transient simulation of physics (i.e., temperature) and biogeochemistry (i.e., export production) over the entire Phanerozoic, we therefore generate 30 model equilibria at regular time intervals throughout the Phanerozoic which are subsequently used as inputs for the regional diversification model (see the Methods section Model coupling).

We employed 30 Phanerozoic palaeogeographic reconstructions through time (~20 Myr evenly spaced time intervals) produced by the plate tectonic/palaeo-elevation model to represent key time periods. For each continental configuration corresponding to a given age in Earth history, we generate idealized 2D wind speed and wind stress, and 1D zonally-averaged albedo forcing fields[47] required by the cGENIE model using the 'muffingen' open-source software (see code availability section below). For each palaeogeographic reconstruction, the climatic forcing (i.e., solar irradiance and carbon dioxide concentration) is adapted to match the corresponding geological time interval. The pCO_2 is taken from the recent update of the GEOCARB model[48]. Solar luminosity is calculated using the model of stellar physics of Gough[49]. We impose modern-day orbital parameters (obliquity, eccentricity and precession). The simulations are initialized with a sea-ice free ocean, homogeneous oceanic temperature (5 °C), salinity (34.9 ‰) and phosphate concentration (2.159 μmol kg^{-1}). Because variations in the oceanic concentration of bio-available phosphate remain challenging to reconstruct in the geological past[50,51], we impose a present-day mean ocean phosphate concentration in our baseline simulations. We quantify the impact of this uncertainty on our model results by conducting additional simulations using half and twice the present-day ocean phosphate concentration (**Extended Data Fig. 11**). For each ocean phosphate scenario (i.e., 0.5×, 1× and 2× the present-day value), each of the 30 model

simulations is then integrated for 20,000 years, a duration ensuring that deep-ocean temperature and geochemistry reach equilibrium. For each model simulation, results of the mean annual values of the last simulated year are used for the analysis. Note that although cGENIE makes projections of the distribution of dissolved oxygen ([O2]) in the ocean, our diversification model does NOT currently consider oxygenation as a limit on diversity. We hence assumed modern atmospheric pCO_2 in all 30 palaeo simulations and did not utilize the resulting projected $[O_2]$ fields.

Regional diversification model

We test two models of diversification, the logistic model and the exponential model, describing the dynamics of regional diversity over time. In both models, the net diversification rate (ρ), with units of inverse time (Myr^{-1}), varies within a pre-fixed range of values as a function of seawater temperature and food availability. The net diversification rate is then calculated for a given location and time according to the following equation:

$$\rho = \rho_{max} - (\rho_{max} - \rho_{min})(1 - Q_{temp} Q_{food}) \qquad \textit{Equation 1}$$

where ρ_{min} and ρ_{max} set the lower and upper net diversification rate limits within which ρ is allowed to vary, and Q_{temp} and Q_{food} are non-dimensional limitation terms with values between 0 and 1 that define the dependence of ρ on temperature and food, respectively (see **Supplementary Table 1**). These temperature and food supply limitation terms vary in space and time as a result of changes in seawater temperature and particulate organic carbon export rate, respectively, thereby controlling the spatial and temporal variability of ρ.

The temperature-dependence of ρ is calculated using the following equation:

$$Q_{temp} = \frac{Q_{10}^{\frac{T - Tmin}{10}}}{Q_{10}^{\frac{Tmax - Tmin}{10}}}$$ *Equation 2*

where the Q_{10} coefficient measures the temperature sensitivity of the origination rate. In the equation 2 above, T is the seawater temperature (in ºC) at a given location and time, while T_{min} and T_{max} are the 0.01 percentile and the 0.99 percentile, respectively, of the temperature frequency distribution in each time interval. In the model, the values of T_{min} and T_{max} used to calculate Q_{temp} are thus recomputed every time interval (~ 5 Myr) according to the temperature frequency distribution of the corresponding time interval. This allows having updated T_{min} and T_{max} in each Phanerozoic time interval and account for the thermal adaptation of organisms to ever-changing climate conditions.

The food limitation term is parameterized using a Michaelis-Menten formulation as follows:

$$Q_{food} = \frac{POC\,flux}{(K_{food} + POC\,flux)}$$ *Equation 3*

where POC flux (mol m^{-2} $year^{-1}$) is the particulate organic carbon export flux, which is used as a surrogate for food availability, at a given location and time of the simulated seafloor. The parameter K_{food} (mol m^{-2} $year^{-1}$) in equation 3 is the half-saturation constant, that is, the POC flux at which the diversification rate is half its maximum value, provided that other factors were not limiting. **Supplementary figure 5** shows the interactive effect of temperature and food supply on net diversification rate for the Q_{10} and K_{food} coefficients used to run the main simulations (i.e. Q_{10} = 1.75, K_{food} = 0.5 mol C $m^{-2}y^{-1}$) and two extreme parameter settings (i.e. Q_{10} = 1.5 and 2.5, K_{food} = 0.25 and 1 mol C $m^{-2}y^{-1}$). **Supplementary figure 6** shows the

spatial variability of the net diversification rate for 6 representative time-slices in the Phanerozoic using the default settings.

The model considers a direct relationship between seawater temperature, food supply and the rate of net diversification based on the theoretical control that temperature and food supply exert on the rates of origination and extinction (**Supplementary Fig. 5)**. Temperature rise is expected to accelerate the biochemical kinetics of metabolism[52] and shorten the development times of individuals[53], leading to higher rates of mutation and origination. Greater food availability increases population sizes, which increases the rates of mutation and reduces the probability of extinction[54]. Furthermore, a large body of observations shows the existence of a positive relationship between resource availability (i.e. food supply) and the standing stock of species in marine and terrestrial communities[55,56]. A larger food supply would support a greater number of individuals. A greater diversity of food resources could also lead to a finer partitioning of resources and a more efficient exploitation of the ecospace.

The net diversification rate becomes negative i) in the event of mass extinctions or ii) in response to regional-scale processes, such as sea-level fall and/or seafloor deformation along convergent plate boundaries. Mass extinction events are imposed as external perturbations to the diversification model by imputing negative net diversification rates to all active seafloor points (ocean points and flooded continental points) and assuming non-selective extinction. The percentage of diversity loss as well as the starting time and duration of mass extinctions are extracted from three fossil diversity curves of reference, namely Sepkoski[21], Alroy[22] and Zaffos et al[23] (**Supplementary Fig. 7**). Each of these fossil diversity curves provides different insights into the Phanerozoic history of marine animal diversity based on uncorrected range-through genus richness estimates[21,23] and sampling standardized estimates[22]. Regional-scale processes, such as sea level fall during marine

regressions and/or seafloor destruction at plate boundaries, either by subduction or uplift, are simulated by the combined plate tectonic/palaeo-elevation model, and constrain the time that seafloor habitats have to accumulate diversity.

The model assumes non-selective extinction during mass extinction events (i.e., the field of bullets model of extinction; everything is equally likely to die, no matter the age of the clade and regardless of adaptation)[57]. However, there is much fossil evidence supporting extinction selectivity[58,59]. It could be argued that higher extinction rates at diversity hotspots would have delayed their subsequent recovery, flattening global diversity trends. This is so considering that, in an exponential diversification model, diversity enhances diversification, leading to a non-linear relationship between the magnitude of diversity loss and the subsequent rebuilding time. This argument is difficult to reconcile with Sepkoski's genus-level global diversity curve but could be consistent with Alroy's standardized diversity curve. Likewise, the model is also not suitable for reproducing the explosive radiations of certain taxonomic groups after mass extinctions, which could explain the offset between the model and fossil observations in the Early Mesozoic (**Fig. 1**).

Letting D represent regional diversity (number of genera within a given seafloor point) and t represent time, the logistic model is formalized by the following differential equation:

$$\frac{\partial D(t)}{\partial t} = \rho D[1 - \frac{D}{K_{eff}}] \qquad \textit{Equation 4}$$

where D(t) is the number of genera at time t and K_{eff} is the effective carrying capacity or maximum number of genera that a given seafloor point (i.e., grid cell area after gridding) can carry at that time, t. In our logistic model, K_{eff} is allowed to vary within a fixed range of values

(from K_{min} to K_{max}) as a positive linear function of the POC flux at a given location and time as follows:

$$K_{eff} = K_{max} - (K_{max} - K_{min}) \frac{\text{POC flux}_{max} - \text{POC flux}}{\text{POC flux}_{max} - \text{POC flux}_{min}} \qquad \textit{Equation 5}$$

where POC $flux_{min}$ and POC $flux_{max}$ corresponds to the 0.01 and 0.99 quantiles of the POC flux range in the whole Phanerozoic dataset.

In the logistic model, the net diversification rate decreases as regional diversity approaches its K_{eff}. The exponential model is a particular case of the logistic model when K_{eff} approaches infinity and, therefore, neither the origination rate nor the extinction rate depend on the standing diversities. In this scenario, diversity grows in an unlimited fashion over time only truncated by the impact of mass extinctions and/or by the dynamics of the seafloor (creation versus destruction). The exponential model is thus as follows:

$$\frac{\partial D(t)}{\partial t} = \rho D \qquad \textit{Equation 6}$$

where the rate of change of diversity (the time derivative) is proportional to the standing diversity *D* such that the regional diversity will follow an exponential increase in time at a speed controlled by the temperature- and food-dependent net diversification rate. Even if analytical solutions exist for the steady-state equilibrium of the logistic and exponential functions, we solved the ordinary differential equations (4) and (6) using numerical methods with a time lag of 1 Myr to account for the spatially- and temporally-varying environmental constraints, seafloor dynamics, and mass extinction events.

Because the analysis of global fossil diversity curves is unable to discern the causes of diversity loss during mass extinctions, our imputation of negative diversification rates could have overestimated the loss of diversity in those cases in which sea level fall, a factor already accounted for by our model, contributed to mass extinction. This effect was particularly recognizable across the Permo-Triassic mass extinction (**Extended Data Fig. 10**), and supports previous claims that the decline in the global area of the shallow water shelf exacerbated the severity of the end-Permian mass extinction[36].

Model coupling

As stated above, the coupled plate tectonic/palaeo-elevation (palaeogeographic) model corresponds to a tracer-based model (a Lagrangian-based approach) that simulates and tracks the spatio-temporal dynamics of ocean and flooded continental points. The diversification models start at time 541 Ma with all active points having a $D_0 = 1$ (one single genus everywhere) and we let points accumulate diversity heterogeneously with time according to seafloor age distributions (for ocean points) and the time that continents have been underwater (for flooded continental points). The ocean points are created at mid-ocean ridges and disappear primarily at subduction zones. Between their origin and demise, the points move following plate tectonic motions and we trace their positions while accumulating diversity. The flooded continental points begin to accumulate diversity from the moment they are submerged, starting with a D value equal to the nearest neighbour flooded continental point with $D > 1$, thereby simulating a process of coastal re-colonization (or immigration). The diversification process remains active while the seafloor points remain underwater, but it is interrupted, and D set to 0, in those continental points that emerge above sea level. Likewise, seafloor points corresponding to ocean domains disappear in subduction zones, and their diversity is lost. We track the geographic position of the ocean and flooded continental points

approximately every 5 Myr, from 541 Ma to the present. Each and every one of the tracked points accumulates diversity over time at a different rate, which is modulated by the environmental history (seawater temperature and food availability) of each point, as described in equations 1-3. When a point arrives in an environment with a carrying capacity lower than the diversity it has accumulated through time, we reset the diversity of the point to the value of the carrying capacity, thereby simulating local extinction.

Seawater temperature (T) and food availability (POC flux) are provided by the cGENIE model, which has a spatial and temporal resolution coarser than the palaeogeographic model. The cGENIE model provides average seawater T and POC flux values in a 36×36 equal area grid (grid cell area equivalent to 2º latitude by 10º longitude at the equator) and 30 time slices or snapshots (from 541 Ma to present: each ~20 Myr time intervals). To have environmental inputs for the 82 time slices of the plate tectonic/palaeo-elevation model, we first interpolate the cGENIE original model output data on a 0.5º by 0.5º grid to match the annotated grids provided by the plate tectonic/palaeo-elevation model. Because the relatively coarse spatial resolution of the cGENIE model prevents rendering the coast-ocean gradients, we assign surface T and POC flux at the base of the euphotic zone to the flooded continental shelf grid cells, and deep ocean T and POC flux at the bottom of the ocean to the ocean grid cells. Because there are time slices without input data of seawater T and POC flux, we inter/extrapolate seawater T and POC flux values into the 0.5º by 0.5º flooded continental shelf and ocean grids independently. Finally, we interpolate values from these 0.5º by 0.5º flooded continental shelf and ocean grids into the exact point locations in each time frame. Therefore, each active point is tracked with its associated time-varying T and POC flux values throughout its lifetime. On average, 6,000 flooded continental points and 44,000 oceanic points were actively accumulating diversity in each time frame. The model cannot simulate the singularities of relatively small enclosed seas for which the spatial resolution of the

palaeogeographic and Earth system models is insufficient to capture relevant features (palaeobathymetry, seawater temperature, etc) in detail. The method is also likely to underestimate the diversity of epeiric (inland) seas due to the difficulty of simulating immigration, a process that is strongly influenced by the effect of marine currents and is not considered here. However, as stated above, the model considers recolonization of recently submerged areas from nearby coastal environments, which partially explains coastal immigration.

Estimation of global diversity from regional diversity

Our regional diversity maps are generated by separately interpolating ocean point diversity and flooded continental point diversity into the 0.5º by 0.5º annotated grids provided by the palaeogeographic model. We calculate global diversity at each time step from each of the regional diversity maps following a series of steps to integrate diversity along line transects from diversity peaks (maxima) to diversity troughs (minima) (**Extended Data Fig. 1**). To select the transects, first, we identify on each of the regional diversity maps the geographic position of the diversity peaks. We identify local maxima (i.e., grid cells with diversity greater than their neighbour cells), and define the peaks as those local maxima with diversity greater than the 0.75 quantile of diversity values in all local maxima in the map. In the case of grid cells with equal neighbour diversity, the peak is assigned to the grid cell in the middle. We subsequently identify the geographic position of the diversity troughs, which are defined as newly formed ocean grid cells (age = 0 Myr) and, therefore, with diversities equal to one. The troughs are mostly located at mid-ocean ridges.

On each of the 82 spatial diversity maps, we trace a line transect from each diversity peak to its closest trough, provided that the transect does not cross land in more than 20 % of the grid

cells along the linear path. On average, for each spatial diversity map, we trace 400 (σ = ±75) linear transects. This sampling design gives rise to transects of different lengths, which may bias the estimates of global diversity. To minimize this bias, we cut the tail of the transects to have a length of 555 km equivalent to 5º at the equator. We test an alternative cutoff threshold; 1110 km, and the results do not alter the study's conclusions.

We apply Bresenham's line algorithm[60] to detect the grid cells crossed by the transects and annotate their diversity. To integrate regional diversity along the transects, we develop a method to simplify the scenario of peaks and troughs heterogeneously distributed on the 2D diversity maps. The method requires i) a vector (the transect) of genus richness (α_n) at n different locations (grids) arranged in a line (1D) of L grids, and ii) a coefficient of similarity ($V_{n,n+1}$) between each two neighbouring locations, n and n+1. $V_{n,n+1}$, the coefficient of similarity, follows a decreasing exponential function with distance between locations. The number of shared genera between n and n+1 is $V_{n,n+1} * \min(\alpha_n; \alpha_{n+1})$. We integrate diversity from peaks to troughs and assume that, along the transect, α_{n+1} is lower than α_n. We further assume that the genera present in n and n+2 cannot be absent from n+1. Using this method, we integrate the transect's diversity (γ_i) using the following equation:

$$\gamma_i = \alpha_1 + \sum_{n=1}^{L-1} (1 - V_{n,n+1}) \alpha_{n+1} \qquad \textit{Equation 7}$$

To integrate the diversity of all transects (γ_i) on each 2D diversity map (or time slice), we apply the same procedure as described above (**Extended Data Fig. 1**). We first sort the transects in descending order from the highest to the lowest diversity. Then, we assume that the number of shared genera between transect i and the rest of the transects with greater diversity {1, 2,…, i -1} is given by the distance of its peak to the nearest neighbour peak [NN(i)] of those already integrated {1,2,… i -1}. Thus, we perform a zigzag integration of

transects' diversities down gradient, from the greatest to the poorest, weighted by the nearest neighbour distance among the peaks already integrated. As a result, the contribution of each transect to global diversity will depend on its diversity and its distance to the closest transect out of all those transects already integrated. With this method, we linearize the problem to simplify the cumbersome procedure of passing from a 2D regional diversity map to a global diversity estimate without knowing the identity (taxonomic affiliation) of the genera. If γ_{total} is the global diversity at time t:

$$\gamma_{total} = \gamma_1 + \sum_{i=2}^{i} (1 - V_{NN(i),i}) \gamma_i \qquad \textit{Equation 8}$$

Finally, the resulting global estimates are plotted against the mid point value of the corresponding time interval to generate a synthetic global diversity curve. In order to compare the global diversity curves produced by the diversification models with those composed from the fossil record, Lin's concordance correlation coefficient (CCC)[24] is applied to the data normalized to the min-max values of each time series (i.e., rescaled within the range 0-1). Lin's CCC combines measures of both precision and accuracy to determine how far the observed data deviate from the line of perfect concordance or gold standard (that is, the 1:1 line). Lin's CCC increases in value as a function of the nearness of the data's reduced major axis to the line of perfect concordance (the accuracy of the data) and of the tightness of the data around its reduced major axis (the precision of the data).

Model parameterization and calibration

The diversification models are parameterized assuming a range of values that constrain the lower and upper limits of the genus-level net diversification rate (ρ_{min} and ρ_{max}, respectively) (**Supplementary Table 1**) according to previously reported estimates from fossil records

(Figures 8 and 11 of Stanley[5]). A range of realistic values is assigned for the parameters Q_{10} and K_{food} (**Supplementary Table 1**), determining, respectively, the thermal sensitivity and food dependence of the net diversification rate. We test a total of 40 different combinations of parameter settings (**Extended Data Table 1**). The resulting estimates of diversity are then compared against the fossil diversity curves of Sepkoski[21], Alroy[22], or Zaffos et al.[23], and the 15 parameter settings providing the highest CCCs are selected.

The results of the logistic diversification model rely on the values of the minimum and maximum carrying capacities (K_{min} and K_{max}, respectively) within which the spatially-resolved effective carrying capacities (K_{eff}) are allowed to vary. The values of K_{min} and K_{max} are thus calibrated by running 28 simulations of pair-wise K_{min} and K_{max} combinations increasing in a geometric sequence of base 2, from 2 to 256 genera (**Extended Data Figs. 3-5**). We perform these simulations independently for each of the 15 parameter settings selected previously (**Extended Data Fig. 6**, **Extended Data Table 1**). Each combination of K_{min} and K_{max} produces a global diversity curve, which is evaluated as described above using Lin's CCC.

Calculating estimates of global diversity from regional diversity maps in the absence of information on genus-level taxonomic identities requires we assume a spatial turnover of taxa with geographic distance (**Extended Data Fig. 1**). Distance–decay curves are routinely fitted by calculating the ecological similarity (e.g. Jaccard similarity index) between each pair of sampling sites, and fitting an exponential decay function to the points on a scatter plot of similarity (y-axis) versus distance (x-axis). Following this method, we fit an exponential decay function to the distance-decay curves reported in Miller et al[61], depicting the decrease in the Jaccard similarity index (J) of fossil genera with geographic distance (great circle distance) at different Phanerozoic time intervals:

$$J = J_{off} + (J_{max} - J_{off})\, e^{\lambda * distance} \qquad \textit{Equation 9}$$

where J_{off} = 0.06 (n.d.) is a small offset, J_{max} = 1.0 (n.d.) is the maximum value of the genus-based Jaccard similarity index, and λ= 0.0024 (Km^{-1}) is the distance-decay rate.

The Jaccard similarity index (J) between consecutive points n and n+1 is bounded between 0 and $\min(\alpha_n; \alpha_{n+1})/\max(\alpha_n; \alpha_{n+1})$. A larger value for J would mean that there are more shared genera between the two communities than there are genera within the least diverse community, which is ecologically absurd. However, using a single similarity decay function can lead the computed value of J to be locally larger than $\min(\alpha_n; \alpha_{n+1}/\max(\alpha_n; \alpha_{n+1})$. To prevent this artefact, we use the Simpson similarity index or "overlap coefficient" (V) instead of J. V corresponds to the percentage of shared genera with respect to the least diverse community ($\min(\alpha_n ; \alpha_{n+1})$). V is bounded between 0 and 1, whatever the ratio of diversities. As the pre-existing estimates of similarity are expressed using J[61], we make the conversion from J to V using the algebraic expression V = (1 + R) * J / (1 + J) where R = $\max(\alpha_n; \alpha_{n+1})/\min(\alpha_n; \alpha_{n+1})$ (see **Annex 1**). In the cases in which J exceeds the $\min(\alpha_n; \alpha_{n+1})/\max(\alpha_n; \alpha_{n+1})$, V becomes > 1 and, in those cases, we force V to be <1 by assuming R = 1, that is $\alpha_n = \alpha_{n+1}$.

The model considers a single distance-decay function for the spatial turnover of taxonomic composition. However, the degree of provinciality (i.e., the partitioning of life into distinct biogeographic units) varies in space and time as a result of environmental gradients[62] and plate tectonics[63]. In fact, the increase in provinciality has been invoked as the main driver of the increase in global diversity, especially in the Late Cretaceous and Cenozoic[23,62,63]. This is a deficiency of the model. Unfortunately, information on the extent to which marine provinciality has varied in space and time throughout the Phanerozoic is limited[61,62], and there

is no simple (mechanistic) way to implement different distance-decay functions of taxonomic similarity in the model. We speculate that including some degree of provincialism in our model could produce the following. There is a clear difference between longitudinal and latitudinal distance, the latter being a more significant source of taxonomic turnover[62]. This effect would add to the observation that tropical diversity hotspots became more prominent towards the end of the Phanerozoic, offering two complementary explanations for the increase in diversity in the Mesozoic: i) favourable conditions for the development of diversity hotspots and ii) a higher degree of provinciality.

Regarding the comparison of model outputs with the fossil record, because the purpose of this modeling study is to reconstruct the unknown dynamics of diversity within regions, we adopted the strategy of spatially integrating regional diversity from our maps and comparing the resulting global diversity curves with the global diversity curves reconstructed from the fossil record (see next section). The comparison between the modelled and fossil global diversity curves is justified by the fact that the dynamics of global diversity should be quantitatively less biased than the dynamics of diversity within regions. Ultimately, our spatially resolved diversification model is intended to provide a benchmark for exploring diversity in those contrasting regions and/or time intervals for which the fossil record is most biased, incomplete, or non-existent. However, it would be interesting to compare the results of the model against the fossil record, at least for those contrasting regions and/or time intervals for which the fossil record is better preserved/sampled. This comparison would allow us to further test the reliability of the model and identify issues from which to improve the model.

Fossil data

We use three fossil diversity curves of reference, namely, Sepkoski, Alroy, and Zaffos et al, in order to i) extract the patterns of mass extinctions (starting time, duration and magnitude) imposed on the model, and ii) compare the global diversity curves produced by the model with those generated from fossil data. Sepkoski's global diversity curve corresponds to marine invertebrates listed in Sepkoski's published marine genus compendium[21] (data downloaded from Sepkoski's Online Genus Database at the following link: http://strata.geology.wisc.edu/jack/). Alroy's and Zaffos et al's global diversity curves are digitized from the original sources, i.e., figure 3 in Alroy[22] and figure 2a in Zaffos et al.[23], respectively. The curve reported by Alroy[22] corresponds to genus-richness estimates obtained after correcting for sampling effort using the shareholder quorum subsampling technique. This curve is binned at approximately 11-Myr time intervals and includes non-tetrapod marine animals of which Anthozoa, Trilobita, Ostracoda, Linguliformea, "Articulata", Bryozoa, Crinoidea, Echinoidea, Graptolithina, Conodonta, Chondrichthyes, Cephalopoda, Gastropoda, and Bivalvia are the major taxonomic groups. The curve reported in Zaffos et al’s study corresponds to 1 Myr range-through richness estimates of marine skeletonized invertebrate genera including Brachiopoda, Bivalvia, Anthozoa, Trilobita, Gastropoda, Crinoidea, Blastoidea, Edrioasteroidea, Ammonoidea, Nautiloidea, and Bryozoa. All digitized (and interpolated) diversity data and the net diversification rate data imputed by the model to simulate mass extinctions are provided as source data files 1 and 2, respectively.

OBIS data

We use the occurrence records of genera belonging to the most diverse marine invertebrate groups: Subphylum Crustacea and Phylum Mollusca, as downloaded from the Ocean Biodiversity Information System (OBIS) on 22nd October 2021 (www.obis.org). The list of genera is validated with the genera names in WoRMS (https://www.marinespecies.org) and

only the accepted, extant and marine names are selected for the analysis. This corresponds to a total of 10,018,142 records of 9,750 genera (6,540,489 records and 5,533 genera of crustaceans and 3,477,653 records and 4,217 genera of molluscs) collected from 1920 to 2021. The records are gridded into hexagons (800,000 km^2 at the equator) to account for different gamma (regional) diversity across latitudes, otherwise, a bias would occur in the resulting estimates. To ensure sufficient sampling size, we select only those hexagons with more than or equal to 10 occurrence records and with more than three genera. Furthermore, we use the frequencies of the genera to estimate the number of unobserved genera per hexagon. We do so by extrapolating the number of genera based on bias-corrected Chao estimate according to the tail of rare genera (i.e., those genera that have only one or two occurrence records in a hexagon)[64,65]. The final number of genera per hexagon is the sum of the observed and unobserved estimates of genera. The analysis is performed with the package "vegan"[66] in R version 4.1.2. Finally, we spatially overlap the hexagons and 0.5x0.5 degrees square grid to match the map of the palaeo analysis and extract the value of the diversity index per coastal grid in QGIS version 3.22.0. The comparison between model and observations is made on the normalised diversities (0-1) bounded between the 0.05 and 0.95 quantiles to minimise the effect of outliers in the observed pattern.

Testing a static (null) palaeogeographic model

In order to evaluate the relative effects of mass extinctions and palaeogeography on global diversity dynamics, we carry out simulations for three static palaeogeographic configurations: the Devonian (400 Ma), the Carboniferous (300 Ma) and the present. For each of these three configurations, the model runs for 541 million years in a 'static mode', that is, diversity accumulates steadily at a pace determined by the temperature and food assigned to each grid at the selected static configuration. Mass extinctions are imposed the same way we do in

the default model with variable palaeogeography. The test is performed for the exponential diversification model and the 'calibrated' logistic model and for each of the three mass extinction patterns (aka Sepkoski, Alroy and Zaffos et al). **Supplementary Figure 2** shows the differences between the log-transformed normalized diversities (between 0 and 1) produced by the diversification models with static palaeogeography (nDiv tectonics OFF) and with variable palaeogeography (nDiv tectonics ON). Red and blue colours denote, respectively, the extent to which the static model produces diversity estimates above or below those produced by the model with plate tectonics. Tropical regions are dominated by reddish colors indicating that the static model particularly overestimates diversity in these regions, where high temperatures accelerate diversification.

In the exponential model, the absence of plate tectonics leads to a scenario of uncontrolled diversity growth (mainly in the tropical shelf seas - reddish areas on maps) that even mass extinctions cannot dampen (**Supplementary Fig. 3a-c**). These results support the idea that Earth's palaeogeographic evolution and sea level changes, by creating, positioning and destroying seafloor habitats, have played a key role in constraining the growth of diversity throughout the Phanerozoic. In the calibrated logistic model (**Supplementary Fig. 3d-f**), regional diversity is constrained by a carrying capacity that prevents diversity from running away. In this case, diversity accumulates in each region at a pace determined by temperature and food until its carrying capacity is reached. Thus, global diversity is steadily increasing over time as a result of the gradual saturation of biological communities within regions.

Additional references

1. Raup, D. M. Species diversity in the Phanerozoic: An interpretation. *Paleobiology* **2**, 289–297 (1976).

2. Sepkoski, J. J. A kinetic model of Phanerozoic taxonomic diversity. III. Post-Paleozoic families and mass extinctions. *Paleobiology* **10**, 246–267 (1984).

3. Alroy, J. *et al.* Phanerozoic trends in the global diversity of marine invertebrates. *Science (80-.).* **321**, 97–100 (2008).

4. Benton, M. J. The Red Queen and the Court Jester: Species diversity and the role of biotic and abiotic factors through time. *Science* vol. 323 (2009).

5. Stanley, S. M. An Analysis of the History of Marine Animal Diversity. *Paleobiology* **33**, 1–55 (2007).

6. MacArthur, R. H. & Wilson, E. O. *The Theory of Island Biogeography.* (Princeton University Press, 1967).

7. Warren, B. H. *et al.* Islands as model systems in ecology and evolution: Prospects fifty years after MacArthur-Wilson. *Ecology Letters* vol. 18 (2015).

8. Benton, M. J. & Emerson, B. C. How did life become so diverse? The dynamics of diversification according to the fossil record and molecular phylogenetics. in *Palaeontology* vol. 50 23–40 (2007).

9. Bush, A. M., Bambach, R. K. & Daley, G. M. Changes in theoretical ecospace utilization in marine fossil assemblages between the mid-Paleozoic and late Cenozoic. *Paleobiology* **33**, 76–97 (2007).

10. Rabosky, D. L. & Hurlbert, A. H. Species richness at continental scales is dominated by ecological limits. *Am. Nat.* **185**, 572–583 (2015).

11. Harmon, L. J. & Harrison, S. Species diversity is dynamic and unbounded at local and continental scales. *Am. Nat.* **185**, 584–593 (2015).

12. Alroy, J. *et al.* Effects of sampling standardization on estimates of Phanerozoic marine diversification. *Proc. Natl. Acad. Sci. U. S. A.* **98**, 6261–6266 (2001).

13. Close, R. A., Benson, R. B. J., Saupe, E. E., Clapham, M. E. & Butler, R. J. The spatial structure of Phanerozoic marine animal diversity. *Science (80-.).* **368**, 420–424 (2020).

14. Peters, S. E. Geologic constraints on the macroevolutionary history of marine animals. *Proc. Natl. Acad. Sci. U. S. A.* **102**, 12326–12331 (2005).

15. Vermeij, G. J. The mesozoic marine revolution: Evidence from snails, predators and grazers. *Paleobiology* **3**, 245–258 (1977).

16. Vermeij, G. J. *Evolution and Escalation*. *Evolution and Escalation* (Princeton University Press, 2021). doi:10.2307/j.ctv18zhf8b.

17. Benton, M. J. Models for the diversification of life. *Trends in Ecology and Evolution* vol. 12 490–495 (1997).

18. Sepkoski, J. J. A kinetic model of Phanerozoic taxonomic diversity II. Early Phanerozoic families and multiple equilibria. *Paleobiology* **5**, 222–251 (1979).

19. Vermeij, G. J. & Leighton, L. R. Does global diversity mean anything? *Paleobiology* **1**, 3–7 (2003).

20. Peters, S. E. & Foote, M. Determinants of extinction in the fossil record. *Nature* **416**, 420–424 (2002).

21. Sepkoski, J. J. J. A compendium of fossil marine animal genera. Edited by David Jablonski and Michael Foote. *Bull. Am. Paleontol.* **363**, 1–560 (2002).

22. Alroy, J. The shifting balance of diversity among major marine animal groups. *Science (80-.).* **329**, 1191–1194 (2010).

23. Zaffos, A., Finnegan, S. & Peters, S. E. Plate tectonic regulation of global marine animal diversity. *Proc. Natl. Acad. Sci. U. S. A.* **114**, 5653–5658 (2017).

24. Lin, L. I.-K. A Concordance Correlation Coefficient to Evaluate Reproducibility. *Biometrics* **45**, 255 (1989).

25. Bradley, D. C. Passive margins through earth history. *Earth-Science Reviews* vol. 91 1–26 (2008).

26. Müller, R. D. *et al.* Ocean Basin Evolution and Global-Scale Plate Reorganization Events since Pangea Breakup. *Annual Review of Earth and Planetary Sciences* vol. 44 107–138 (2016).

27. Hannisdal, B. & Peters, S. E. Phanerozoic earth system evolution and marine biodiversity. *Science (80-.).* **334**, 1121–1124 (2011).

28. Erwin, D. H. Climate as a Driver of Evolutionary Change. *Current Biology* vol. 19 (2009).

29. Valentine, J. W. & Moores, E. M. Plate-tectonic regulation of faunal diversity and sea level: A model. *Nature* **228**, 657–659 (1970).

30. Valentine, J. W. & Moores, E. M. Global Tectonics and the Fossil Record. *J. Geol.* **80**, 167–184 (1972).

31. Bush, A. M. & Bambach, R. K. Paleoecologic megatrends in marine metazoa. *Annu. Rev. Earth Planet. Sci.* **39**, (2011).

32. Bush, A. M., Hunt, G. & Bambach, R. K. Sex and the shifting biodiversity dynamics of marine animals in deep time. *Proc. Natl. Acad. Sci. U. S. A.* **113**, (2016).

33. Hoyal Cuthill, J. F., Guttenberg, N. & Budd, G. E. Impacts of speciation and extinction measured by an evolutionary decay clock. *Nature* **588**, (2020).

34. Merdith, A. S. *et al.* Extending full-plate tectonic models into deep time: Linking the Neoproterozoic and the Phanerozoic. *Earth-Science Reviews* vol. 214 (2021).

35. Scotese, C. R. & Wright, N. PALEOMAP Paleodigital Elevation Models (PaleoDEMS) for the Phanerozoic PALEOMAP Project, https://www.earthbyte.org/paleodem-resource-scotese-and-wright-2018/. (2018).

36. Scotese, C. R. An atlas of phanerozoic paleogeographic maps: The seas come in and the seas go out. *Annual Review of Earth and Planetary Sciences* vol. 49 679–728 (2021).

37. Kocsis, Á. T. & Scotese, C. R. Mapping paleocoastlines and continental flooding during the Phanerozoic. *Earth-Science Reviews* vol. 213 103463 (2021).

38. Markwick, P. J. & Valdes, P. J. Palaeo-digital elevation models for use as boundary conditions in coupled ocean - Atmosphere GCM experiments: A Maastrichtian (late Cretaceous) example. *Palaeogeogr. Palaeoclimatol. Palaeoecol.* **213**, (2004).

39. Boulila, S., Laskar, J., Haq, B. U., Galbrun, B. & Hara, N. Long-term cyclicities in Phanerozoic sea-level sedimentary record and their potential drivers. *Glob. Planet. Change* **165**, (2018).

40. Müller, R. D., Sdrolias, M., Gaina, C., Steinberger, B. & Heine, C. Long-term sea-level fluctuations driven by ocean basin dynamics. *Science (80-.).* **319**, 1357–1362 (2008).

41. Williams, S., Wright, N. M., Cannon, J., Flament, N. & Müller, R. D. Reconstructing seafloor age distributions in lost ocean basins. *Geosci. Front.* **12**, 769–780 (2021).

42. Cao, W. *et al.* Improving global paleogeography since the late Paleozoic using paleobiology. *Biogeosciences* **14**, 5425–5439 (2017).

43. Ridgwell, A. *et al.* Marine geochemical data assimilation in an efficient Earth system model of global biogeochemical cycling. *Biogeosciences* **4**, 87–104 (2007).

44. Ward, B. A. *et al.* EcoGEnIE 1.0: Plankton ecology in the cGEnIE Earth system model. *Geosci. Model Dev.* **11**, 4241–4267 (2018).

45. Wilson, J. D., Monteiro, F. M., Schmidt, D. N., Ward, B. A. & Ridgwell, A. Linking Marine Plankton Ecosystems and Climate: A New Modeling Approach to the Warm Early Eocene Climate. *Paleoceanogr. Paleoclimatology* **33**, 1439–1452 (2018).

46. Crichton, K. A., Wilson, J. D., Ridgwell, A. & Pearson, P. N. P. N. Calibration of temperature-dependent ocean microbial processes in the cGENIE.muffin (v0.9.13) Earth system model. *Geosci. Model Dev.* **14**, 125–149 (2021).

47. Vervoort, P., Kirtland Turner, S., Rochholz, F. & Ridgwell, A. Earth System Model Analysis of How Astronomical Forcing Is Imprinted Onto the Marine Geological Record: The Role of the Inorganic (Carbonate) Carbon Cycle and Feedbacks. *Paleoceanogr. Paleoclimatology* **36**, (2021).

48. Krause, A. J. *et al.* Stepwise oxygenation of the Paleozoic atmosphere. *Nat. Commun.* **9**, (2018).

49. Gough, D. O. Solar interior structure and luminosity variations. *Sol. Phys.* **74**, 21–34 (1981).

50. Reinhard, C. T. *et al.* Evolution of the global phosphorus cycle. *Nature* **541**, 386–389 (2017).

51. Wang, R. *et al.* The coupling of Phanerozoic continental weathering and marine phosphorus cycle. *Sci. Rep.* **10**, (2020).

52. Allen, A. P., Brown, J. H. & Gillooly, J. F. Global biodiversity, biochemical kinetics, and the energetic-equivalence rule. *Science (80-.).* **297**, (2002).

53. Gillooly, J. F., Charnov, E. L., West, G. B., Savage, V. M. & Brown, J. H. Effects of size and temperature on developmental time. *Nature* **417**, (2002).

54. Pimm, S. L., Jones, H. L. & Diamond, J. On the risks of extinction. *Am. Nat.* **132**, (1988).

55. Tilman, D. The ecological consequences of changes in biodiversity: A search for general principles. in *Ecology* vol. 80 (1999).

56. Costello, M. J. & Chaudhary, C. Marine Biodiversity, Biogeography, Deep-Sea Gradients, and Conservation. *Current Biology* vol. 27 (2017).

57. Raup, D. Extinction: bad genes or bad luck? *New Sci.* **131**, (1991).

58. Peters, S. E. Environmental determinants of extinction selectivity in the fossil record. *Nature* **454**, (2008).

59. Payne, J. L. *et al.* Extinction intensity, selectivity and their combined macroevolutionary influence in the fossil record. *Biol. Lett.* **12**, (2016).

60. Bresenham, J. E. Algorithm for computer control of a digital plotter. *IBM Syst. J.* **4**, 25–30 (2010).

61. Miller, A. I. *et al.* Phanerozoic trends in the global geographic disparity of marine biotas. *Paleobiology* **35**, 612–630 (2009).

62. Kocsis, Á. T., Reddin, C. J., Scotese, C. R., Valdes, P. J. & Kiessling, W. Increase in marine provinciality over the last 250 million years governed more by climate change than plate tectonics. *Proc. R. Soc. B Biol. Sci.* **288**, (2021).

63. Valentine, J. W., Foin, T. C. & Peart, D. A provincial model of Phanerozoic marine diversity. *Paleobiology* **4**, 55–66 (1978).

64. O'Hara, R. B. Species richness estimators: How many species can dance on the head of a pin? *J. Anim. Ecol.* **74**, (2005).

65. Chiu, C. H., Wang, Y. T., Walther, B. A. & Chao, A. An improved nonparametric lower bound of species richness via a modified good-turing frequency formula. *Biometrics* **70**, (2014).

66. Oksanen, J. *et al.* Package 'vegan' Title Community Ecology Package Version 2.5-7. *R* **2.5**, (2020).

Code Availability

The coupled palaeogeographic-diversification model presented here uses input data of seafloor age distributions and palaeoenvironmental conditions from the siwill22/agegrid-0.1 v1-alpha palaeogeographic model and the cGENIE Earth System Model, respectively. We provide code availability for each of these two models. The code for the palaeogeographic model reconstructing seafloor age distributions from GPlates full-plate tectonic reconstructions is assigned a DOI: 10.5281/zenodo.3271360. The code for the version of the 'muffin' release of the cGENIE Earth System Model used in this study, is tagged as v0.9.20, and is assigned a DOI: 10.5281/zenodo.4618023.

The code and data for the coupled palaeogeographic-diversification (INDITEK) model are available on GitHub (https://github.com/CarmenGarciaComas/INDITEK, last access: October 2021).The model is written in MATLAB 2013b and tested with MATLAB 2021a in a MacOS 2.3 GHz 8-Core Intel Core i9, and with MATLAB 2020b on Windows with a 2.5 GHz Intel i5-3210M and on Linux Debian with a 2.6 GHz Intel Core 9th Gen i9-9980HK processor. A manual (README.md) detailing the main code modules, basic model configuration, input data files (including those required from the palaeogeographic model and the cGENIE Earth System model simulations), and how to run the model and plot the results is provided through the link above.

Acknowledgements

This work was funded by research grant CGL2017-91489-EXP (INDITEK project) from the Spanish government. A.P. acknowledges funding from the European Union's Horizon research and innovation programme under the Marie Sklodowska-Curie grant agreement No. 838373. A.R. acknowledges NSF grant EAR-2121165, as well as support from the Heising-Simons Foundation. M.J.B. acknowledges support through ERC Advanced Grant 'Innovation'

(ERC 788203). P.C. and S.M.V. acknowledge support through CTM2017-87227-P grant from the Spanish government. P.C., C.G-C. and G.L. acknowledge support for the publication fee by the CSIC Open Access Publication Support Initiative through its Unit of Information Resources for Research (URICI).

Author contributions

P.C. and C.G-C. proposed and designed the study. P.C., C.G-C. and S.M.V. developed the diversification model. A.P. and A.R. performed the cGENIE model simulations. S.W. and R.D.M. prepared the plate tectonic/palaeo-elevation model reconstructions. C.G-C. performed the coupling of the diversification model to the plate tectonic/paleo-elevation model. C.G-C. and G.L-G. developed the method to estimate global diversity from regional diversity. C.C. analysed OBIS data for marine invertebrates. P.C., C.G-C., A.P., S.W., M.J.B., C.C, G.L-G., R.D.M., A.R. and S.M.V. contributed to data analysis and discussion of results. P.C., C.G-C., A.P., S.W. wrote the manuscript with inputs from all authors.

Competing interests

The authors declare no competing interests.

Supplementary Information is available for this paper.

Correspondence and requests for materials should be addressed to P.C. (pedrocermeno@icm.csic.es) and/or C.G-C. (cgcomas@icm.csic.es)

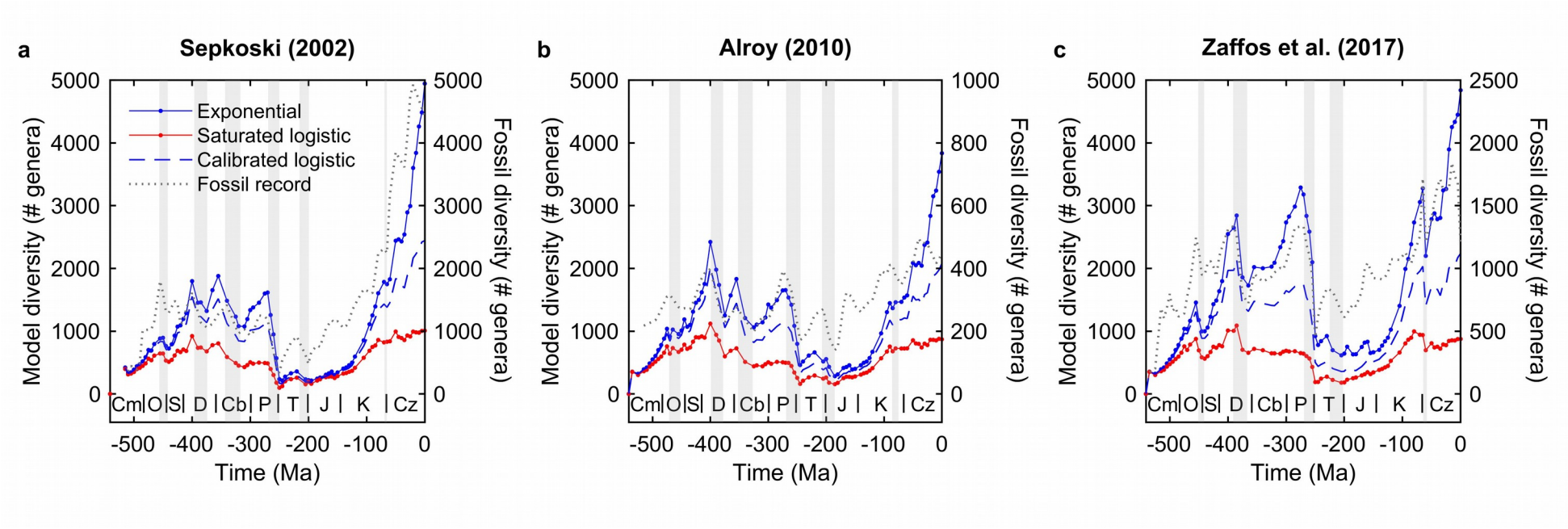

FIGURE 1: Global diversity dynamics across the Phanerozoic.

a-c, Global diversity dynamics reconstructed from the 'saturated' logistic model (red), the exponential model (blue) and the 'calibrated' logistic model (blue dashed line, see Figure 2 for calibration) after imposing the pattern of mass extinctions of Sepkoski[21] (**a**), Alroy[22](**b**), and Zaffos et al.[23] (**c**). In each panel, the corresponding fossil diversity curve is superimposed (grey). Cm, Cambrian; O, Ordovician; S, Silurian; D, Devonian; Cb, Carboniferous; P, Permain; T, Triassic; J, Jurassic; K, Cretaceous; Cz, Cenozoic. Shaded areas represent mass extinctions.

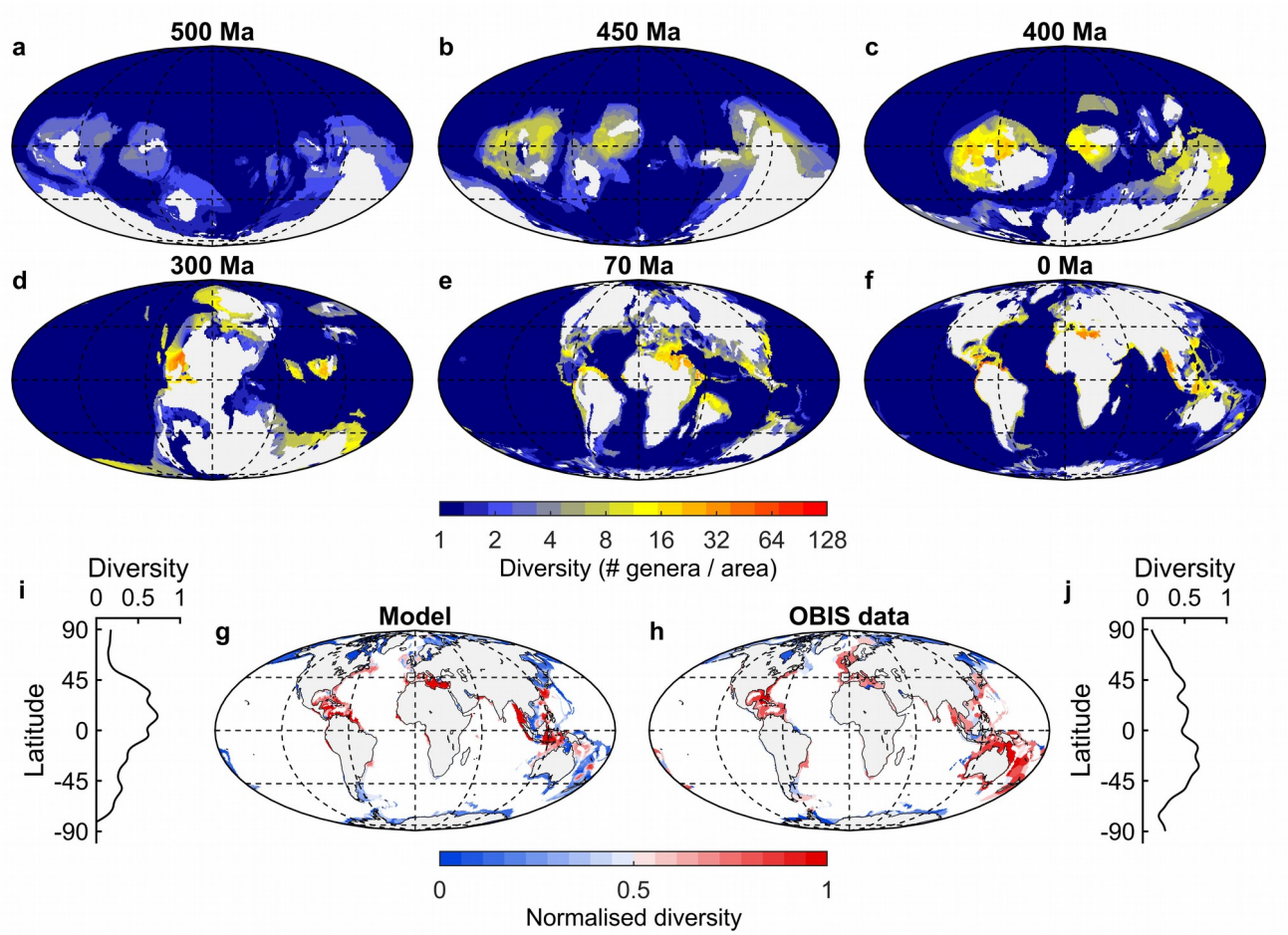

927 **FIGURE 2: Re-diversifying the Phanerozoic oceans.**
928 **a-f,** Spatial distribution of marine animal diversity (# genera / area) in the Cambrian
929 (Guzhangian, 500 Ma), Late Ordovician (Katian, 450 Ma), Early Devonian (Emsian, 400 Ma),
930 Late Carboniferous (Pennsylvanian, 300 Ma), Late Cretaceous (Maastrichtian, 70 Ma) and
931 present generated by the calibrated logistic model after imposing the pattern of mass
932 extinctions extracted from the fossil diversity curve of Sepkoski[21]. This model run uses the
933 following parameters: Q_{10} = 1.75, K_{food} = 0.5 molC $m^{-2}y^{-1}$, net diversification rate limits (ρ_{min} -
934 ρ_{max}) = 0.001-0.035 Myr^{-1} (per capita), and a K_{min} to K_{max} range between 12 and 123 genera
935 per unit area according to the calibration analysis presented in **Extended Data Fig. 6**. The
936 same plots but for the mass extinction patterns extracted from the fossil diversity curves of
937 Alroy[22] and Zaffos et al[23] are shown in **Extended Data Figs. 7-8**. See **Supplementary Video**
938 **3** for the full Phanerozoic sequence. **g-h,** Current spatial distributions of diversity along the
939 continental margins from model simulations and observations extracted from the Ocean
940 Biodiversity Information System (OBIS) database (genera belonging to Subphyllum
941 Crustacea and Phyllum Mollusca). For the purpose of comparison, normalized diversities (0-

1) bounded between quantiles 0.05 and 0.95 are represented. **i-j**, Latitudinal distributions of diversity averaged in 10 degree zonal bands.

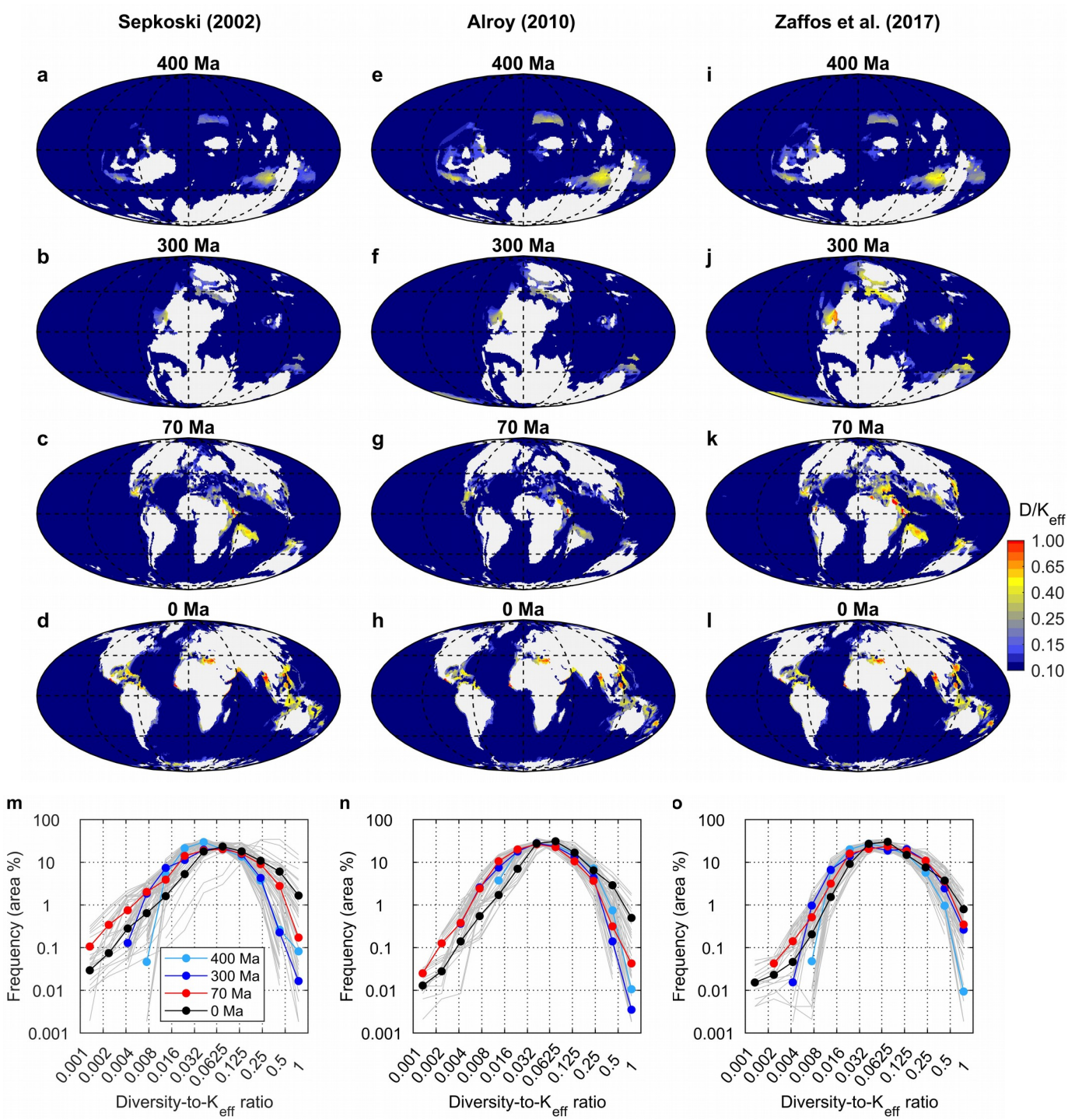

FIGURE 3: The pervasiveness of ecological unsaturation.

Spatial distribution of the diversity-to-carrying capacity (K_{eff}) ratio (colourbar) in deep sea habitats and flooded continental regions of the Early Devonian (Emsian, 400 Ma), Late Carboniferous (Pennsylvanian, 300 Ma), Late Cretaceous (Maastrichtian, 70 Ma) and present using the 'calibrated' logistic model after imposing the mass extinction patterns of Sepkoski[21] (**a-d**), Alroy[22] (**e-h**), and Zaffos et al[23] (**i-l**). See **Supplementary Video 4** for the full

Phanerozoic sequences. **m-o**, Frequency distributions (% area) of the diversity-to-K_{eff} ratio for the flooded continental regions. The grey lines are frequency distributions generated from simulations using the 15 different parameter settings listed in **Extended Data Table 1**. The colour dots are average values for different Phanerozoic times.

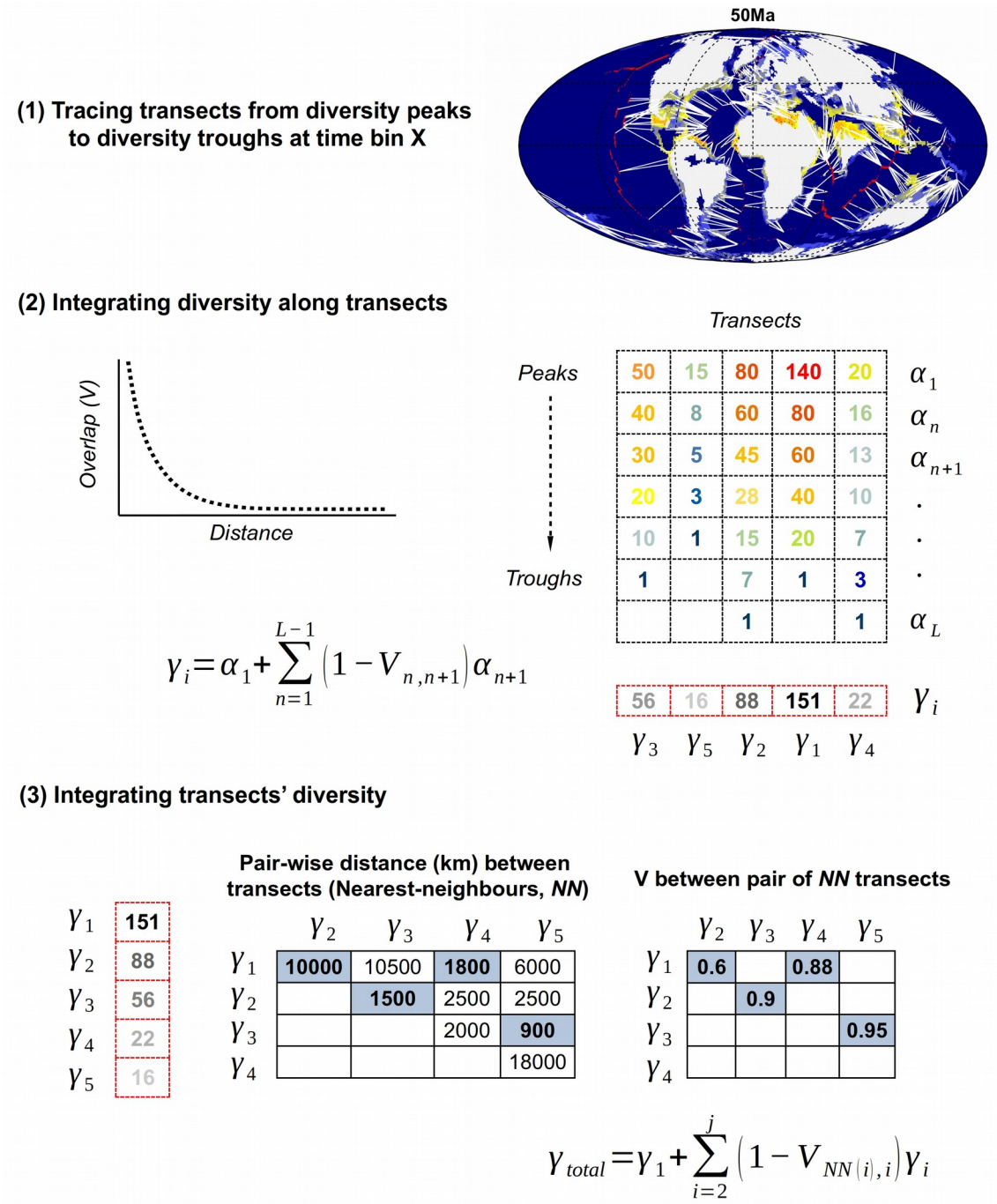

EXTENDED DATA FIGURE 1: Computing global diversity from diversity maps. For each time interval or regional diversity map, (1) we plot hundreds of transects (white lines) from diversity peaks to their nearest troughs, (2) we integrate diversity along the transects (from α_n to α_L) according to the distance between pairs of grids using the overlap coefficient (V), which gives the proportion of shared genera with respect to the grid with the least diversity, i.e. $V_{n,n+1} * \min(\alpha_n; \alpha_{n+1})$ [see Annex 1], (3) we order the resulting transects' diversity (γ_i) from maximum diversity (γ_{max}) to minimum diversity (γ_{min}), calculate the pair-wise

distance between transects (the distance between their peaks), and integrate the diversity of transects from the greatest to lowest according to the nearest-neighbour distance of the corresponding transect to those transects already integrated (γ_{total}).

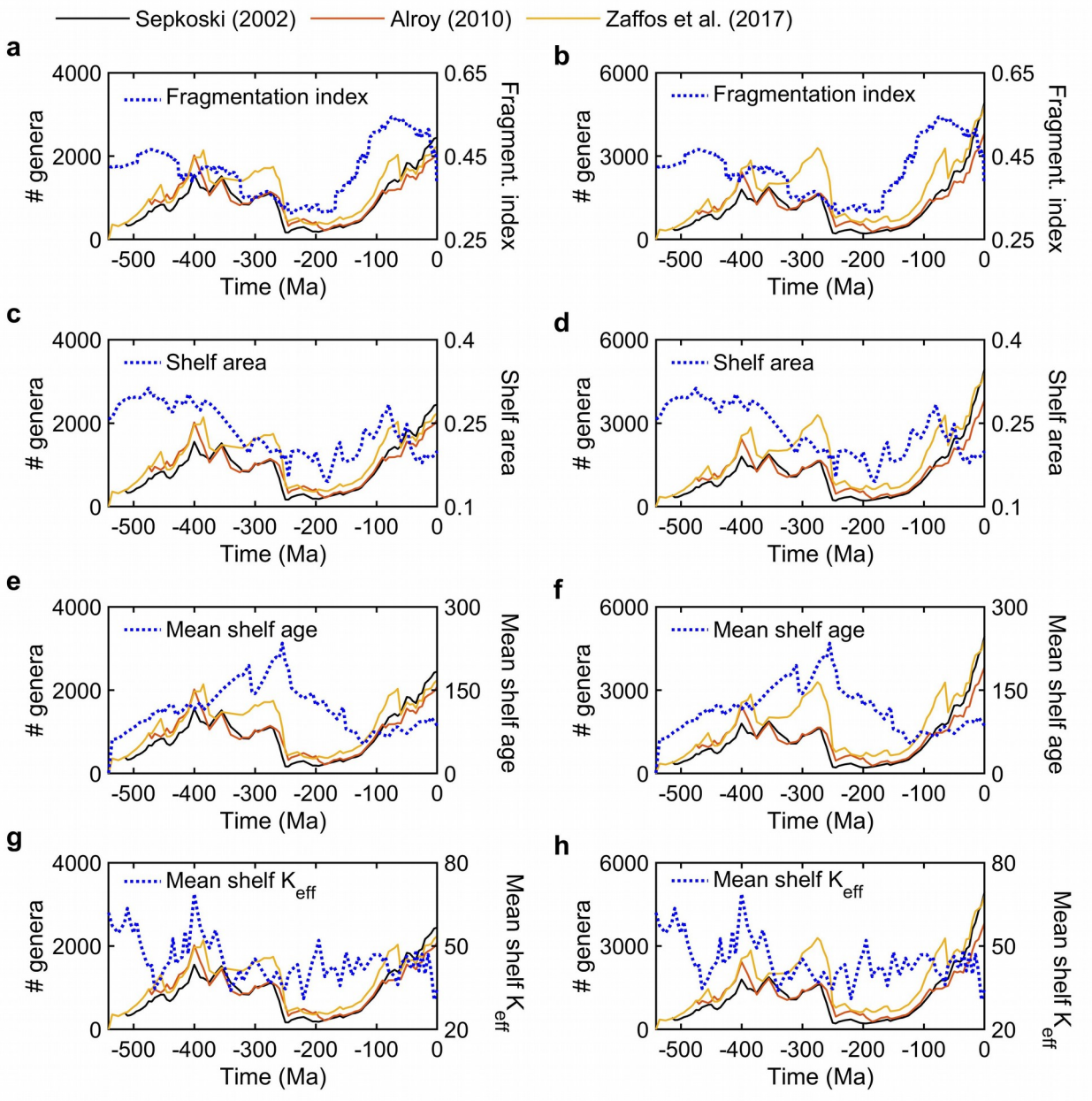

964 **EXTENDED DATA FIGURE 2: Continental configuration and global diversity dynamics.**
965 **a-f,** Global diversity dynamics (# genera) reconstructed from the 'calibrated' logistic model (**a,**
966 **c, e**) and the exponential model (**b, d, f**) overimposed on the temporal variability of the
967 fragmentation index (**a, b**), global mean shelf area (**c, d**), mean shelf age (**e, f**) and mean
968 shelf K_{eff} (**g, h**).

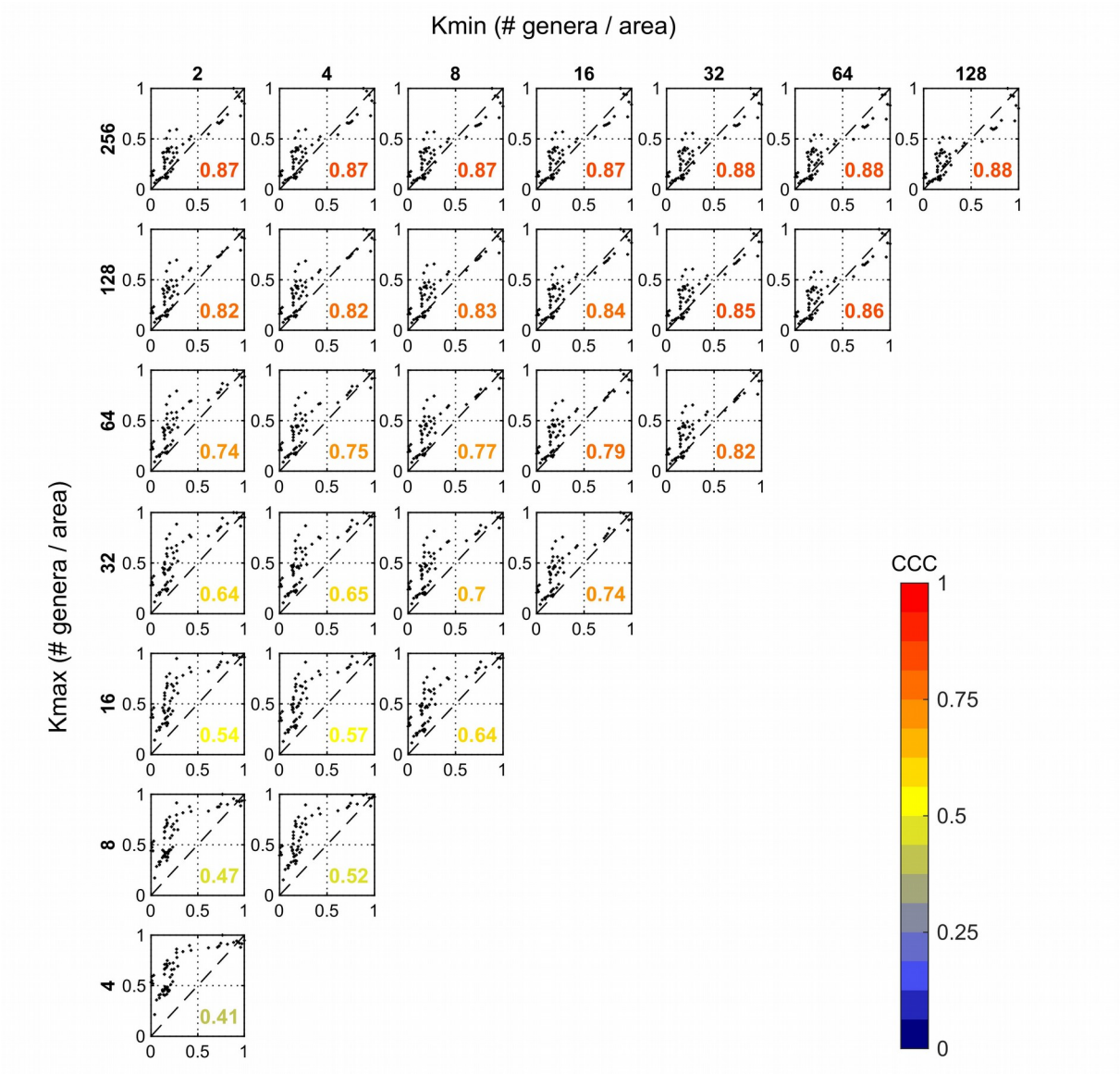

EXTENDED DATA FIGURE 3: Calibrating the K_{min} and K_{max} values of the logistic model. Normalized model diversity (0-1) versus normalized fossil diversity (0-1) for different combinations of the K_{min} and K_{max} values of the model. These simulations use the pattern of mass extinctions extracted from the fossil diversity curve of Sepkoski[21]. Lin's Concordance Correlation coefficient (CCC), which quantifies the alignment of the model estimates to the 1:1 line, is shown in each panel with colour code.

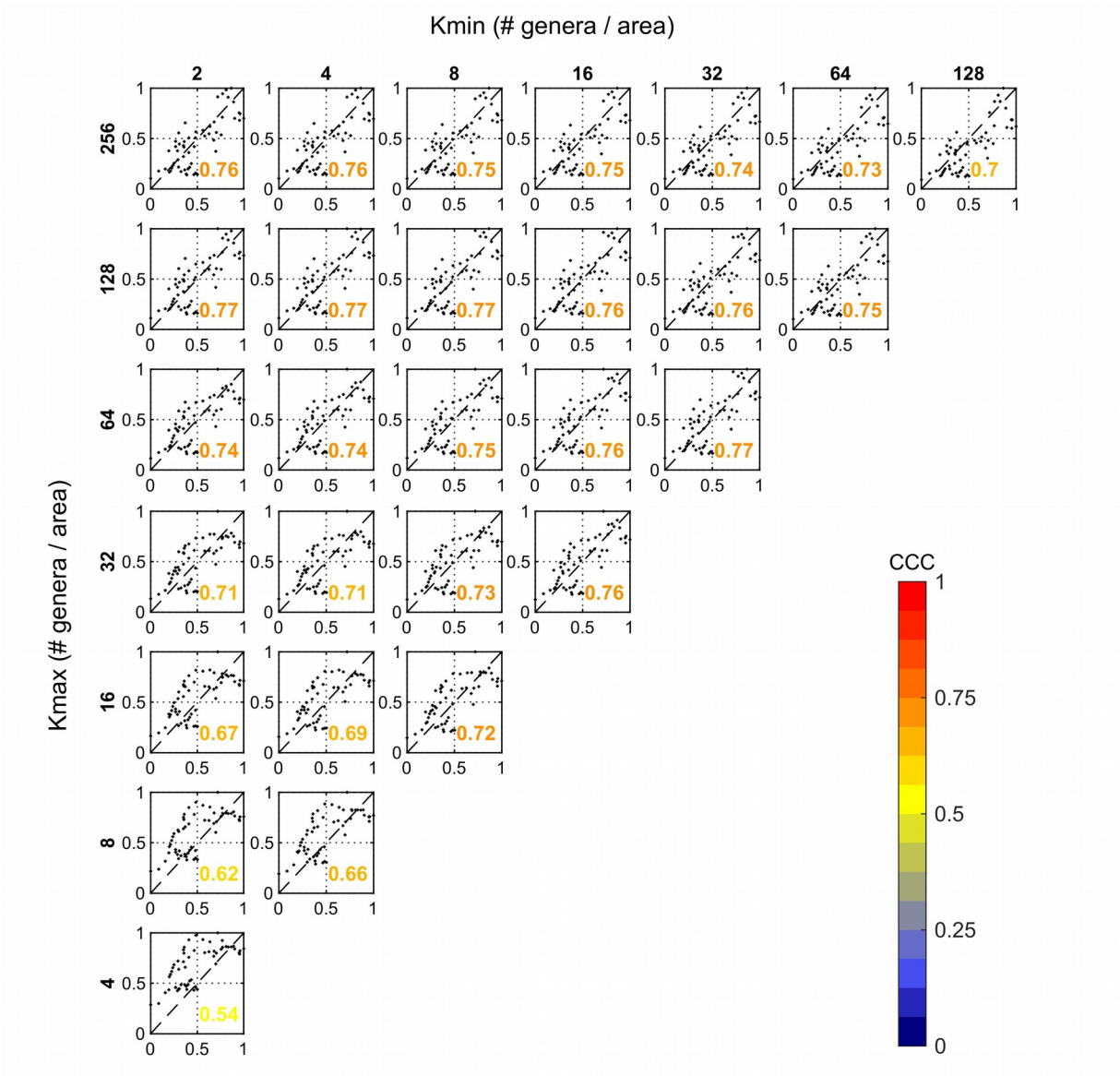

EXTENDED DATA FIGURE 4: Calibrating the K_{min} and K_{max} values of the logistic model. As Extended Data Figure 3 but for the pattern of mass extinctions extracted from the fossil diversity curve of Alroy[22], and the fossil diversity estimates reported in Alroy[22].

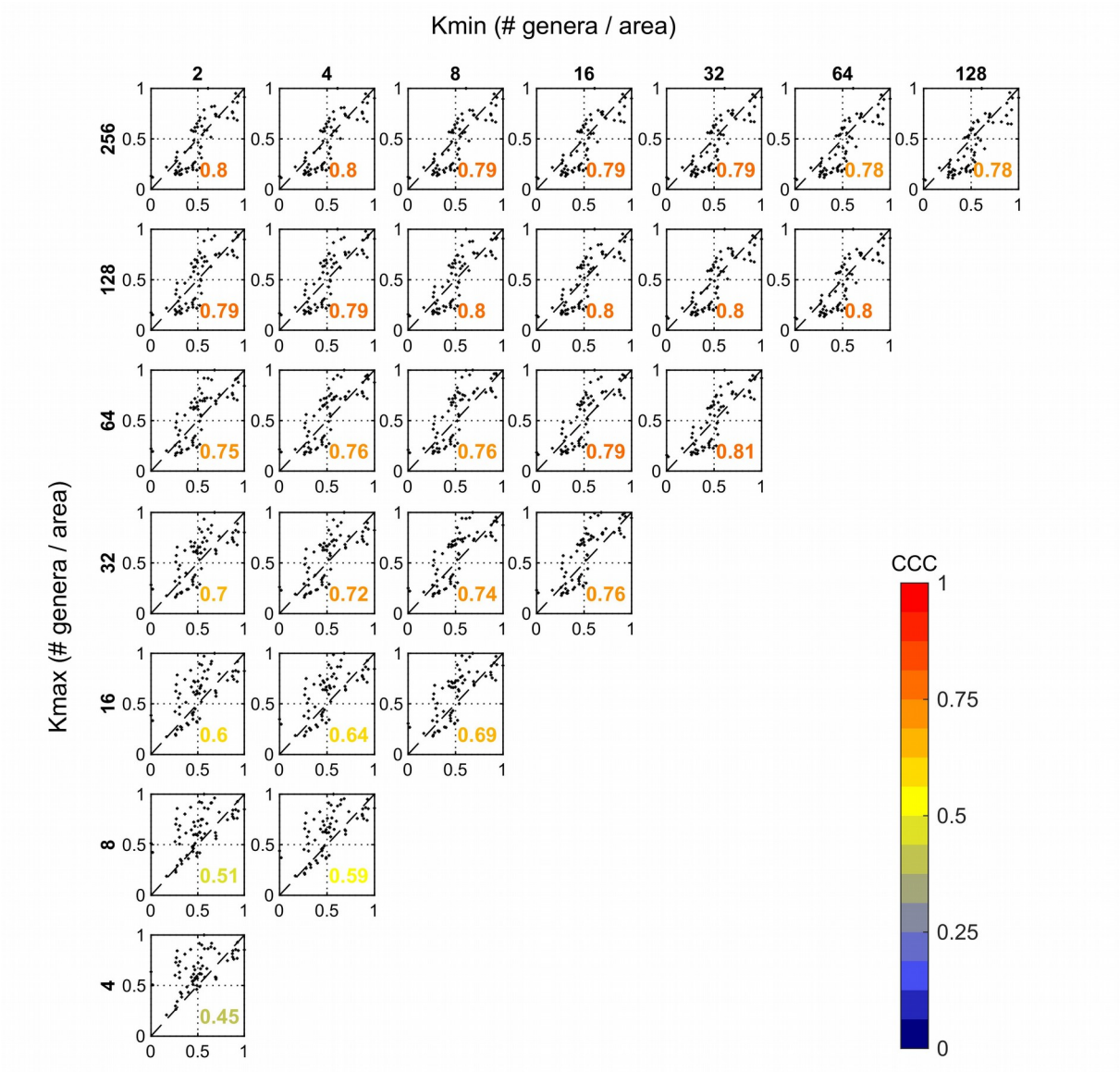

EXTENDED DATA FIGURE 5: Calibrating the K_{min} and K_{max} values of the logistic model. As Extended Data Figure 3 but for the pattern of mass extinctions extracted from the fossil diversity curve of Zaffos et al[23] and the fossil diversity estimates reported in Zaffos et al[23].

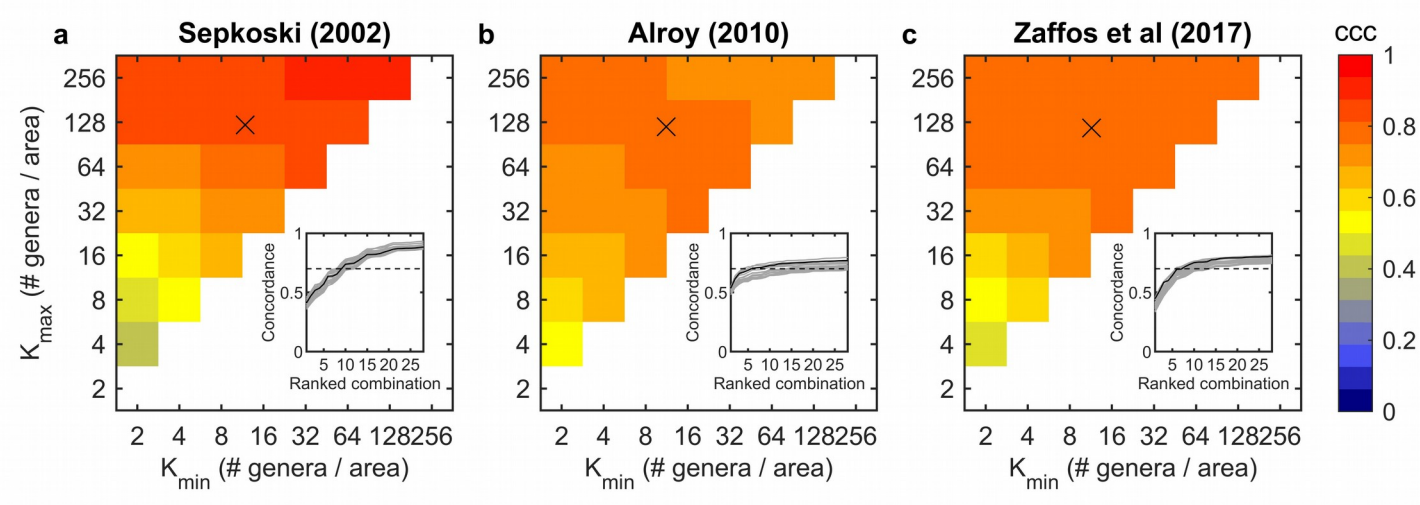

EXTENDED DATA FIGURE 6: Calibrating the logistic model's carrying capacities. a-c, Lin's concordance correlation coefficients (CCC) for the relationship between the global diversities resulting from the model and the fossil diversity estimates of Sepkoski[21] (**a**), Alroy[22] (**b**), and Zaffos et al[23] (**c**) using different combinations of K_{min} and K_{max} in the model (**Extended Data Figs. 3-5** for details on correlations). The inset in each panel shows the CCCs in ascending order for the different combinations of K_{min} and K_{max}. The black curve in the insets is for the simulation run using the selected parameters (**Supplementary Table 1**). The grey curves are for each of the first 15 combinations of parameters listed in **Extended Data Table 1**. The dashed line denotes the CCC value of 0.7 and the cross in each panel is the average of all K_{min} and K_{max} combinations giving a CCC greater than 0.7. These are the values of K_{min} and K_{max} used to run the 'calibrated' logistic model.

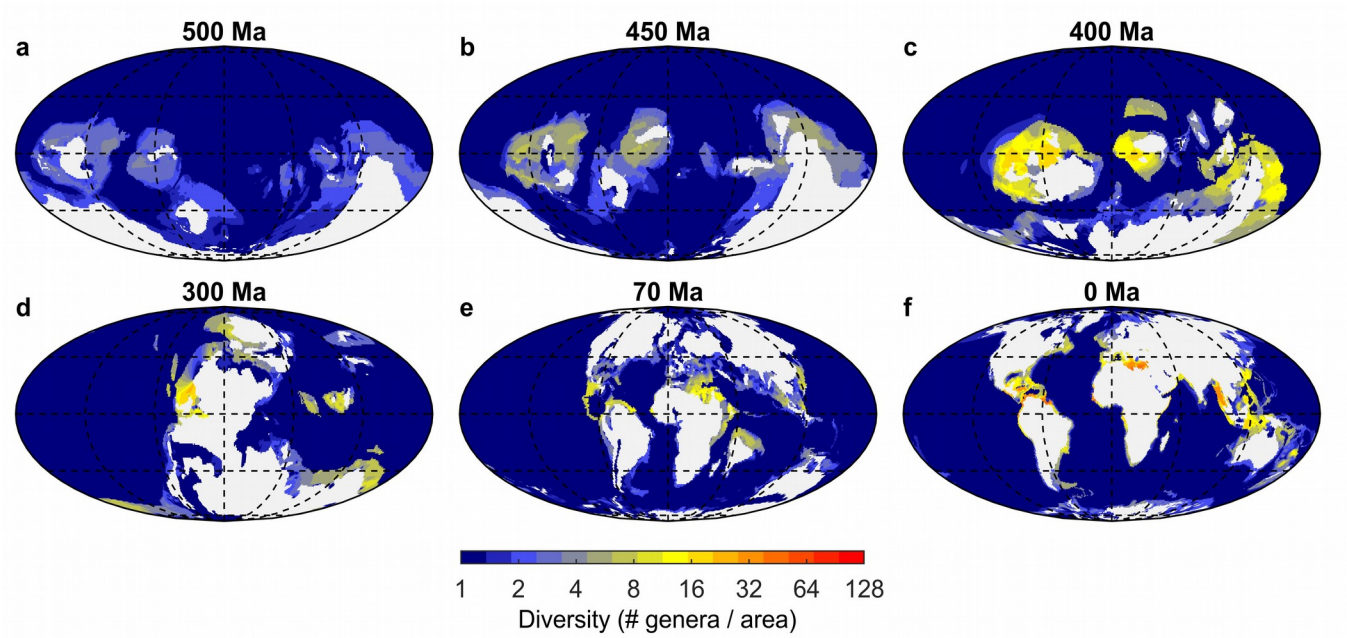

EXTENDED DATA FIGURE 7: Re-diversifying the Phanerozoic oceans. **a-f,** Spatial distribution of marine animal diversity (# genera / area) in the Cambrian (Guzhangian, 500 Ma), Late Ordovician (Katian, 450 Ma), Early Devonian (Emsian, 400 Ma), Late Carboniferous (Pennsylvanian, 300 Ma), Late Cretaceous (Maastrichtian, 70 Ma) and present generated by the calibrated logistic model after imposing the pattern of mass extinctions extracted from the fossil diversity curve of Alroy[22]. These model runs use the following parameters: Q_{10} = 1.75, K_{food} = 0.5 molC $m^{-2}y^{-1}$, net diversification rate limits (ρ_{min} - ρ_{max}) = 0.001-0.035 Myr^{-1} (per capita), and a K_{min} to K_{max} range between 11 and 119 genera per unit area. These carrying capacity values are derived from the analysis presented in **Extended Data Fig. 6**. See also **Supplementary Video 3** for the full Phanerozoic sequence.

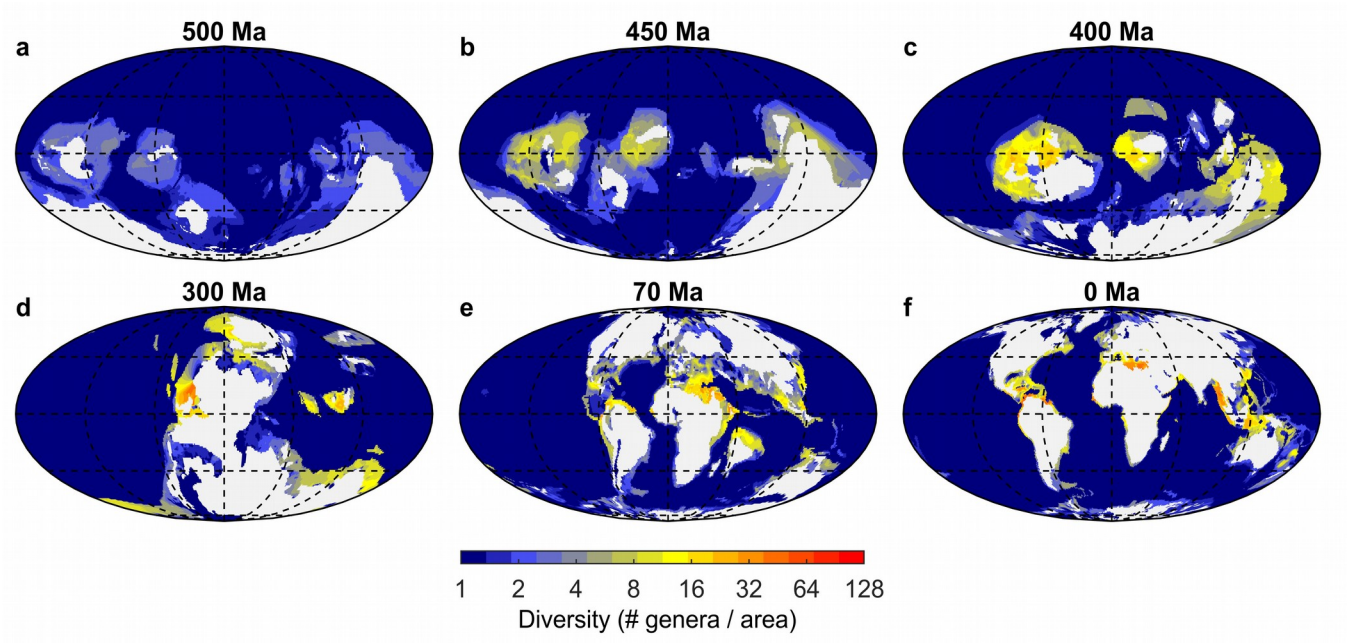

EXTENDED DATA FIGURE 8: Re-diversifying the Phanerozoic oceans.

a-f, Spatial distribution of marine animal diversity (# genera / area) in the Cambrian (Guzhangian, 500 Ma), Late Ordovician (Katian, 450 Ma), Early Devonian (Emsian, 400 Ma), Late Carboniferous (Pennsylvanian, 300 Ma), Late Cretaceous (Maastrichtian, 70 Ma) and present generated by the calibrated logistic model after imposing the pattern of mass extinctions extracted from the fossil diversity curve of Zaffos et al.[23] {Formatting Citation}. These model runs use the following parameters: Q_{10} = 1.75, K_{food} = 0.5 molC $m^{-2}y^{-1}$, net diversification rate limits (ρ_{min} - ρ_{max}) = 0.001-0.035 Myr^{-1} (per capita), and a K_{min} to K_{max} range between 11 and 117. These carrying capacity values are derived from the analysis presented in **Extended Data Fig. 6**. See also **Supplementary Video 3** for the full Phanerozoic sequence.

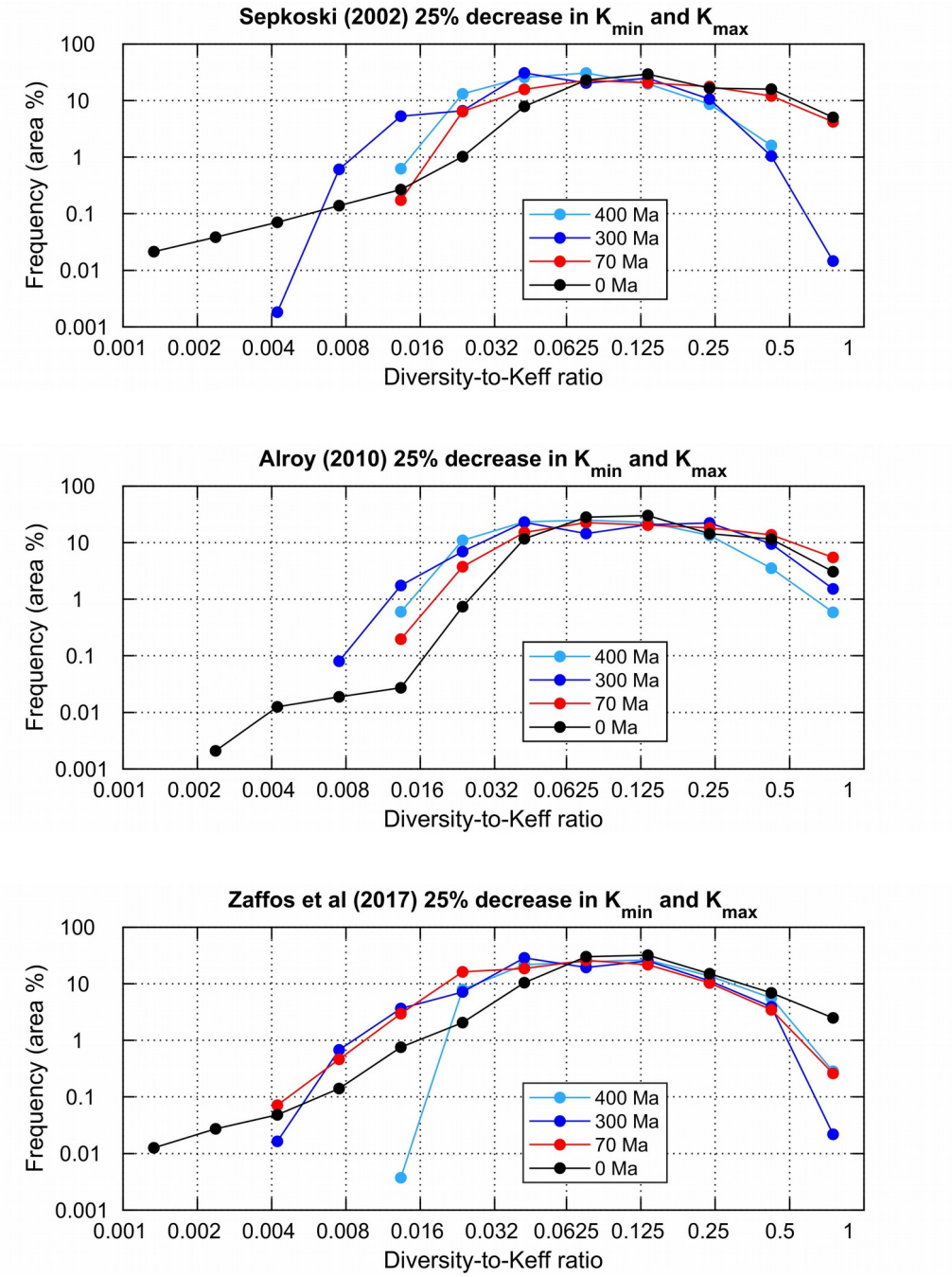

EXTENDED DATA FIGURE 9: Robustness of the diversity-to-K_{eff} frequency distribution pattern. Frequency distributions (% area) of the diversity-to-K_{eff} ratio for the flooded continental regions after decreasing the values of K_{min} and K_{max} in the model by 25% with respect to the calibrated values [i.e., 12-123 (for Sepkoski), 11-119 (for Alroy), 11-117 (for Zaffos et al)].

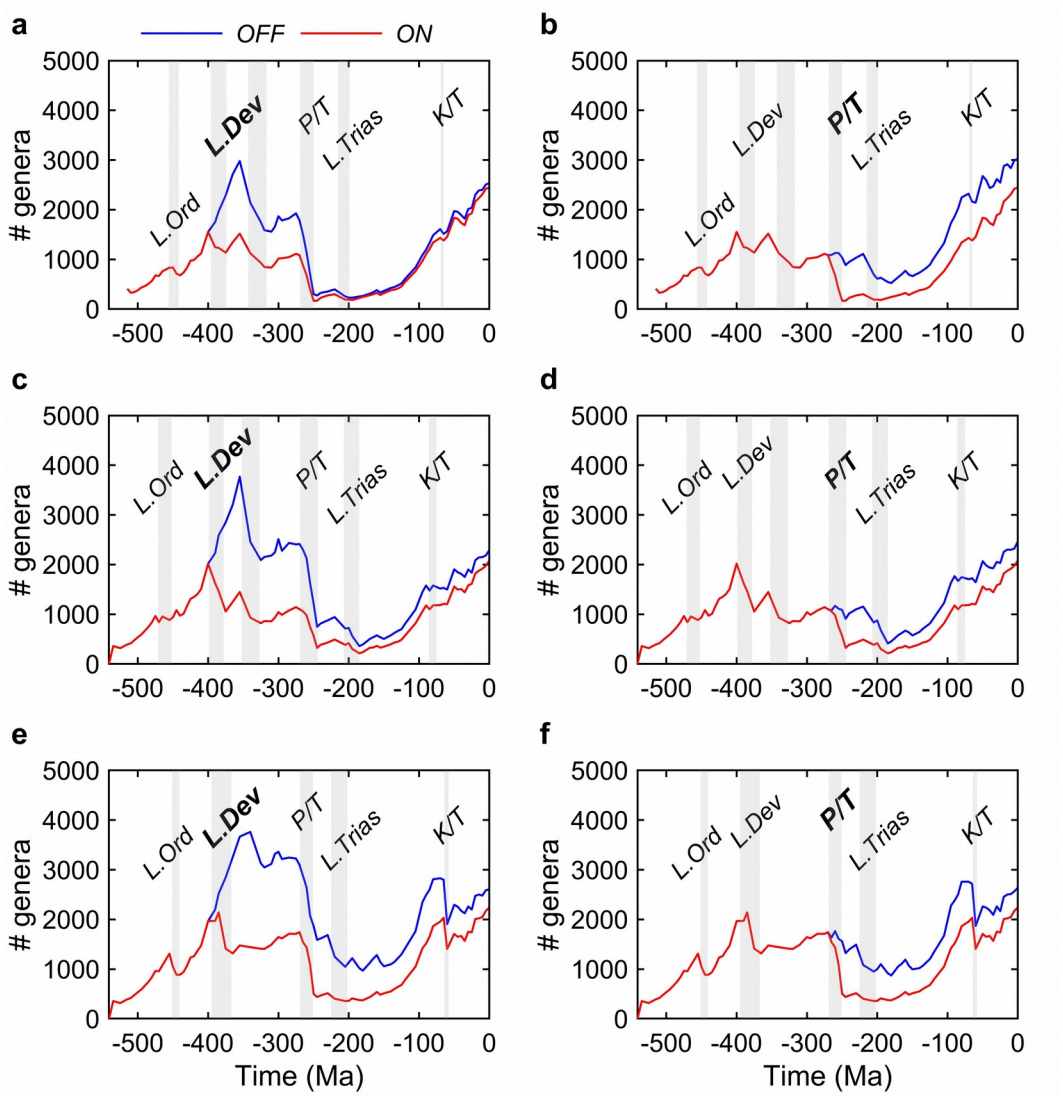

EXTENDED DATA FIGURE 10: Testing the effect of enabling/disabling mass extinctions. Global diversity (# genera) trajectories reconstructed from the calibrated logistic model after disabling (blue) and enabling (red) the Late Devonian and Permo-Triassic mass extinctions from the mass extinction pattern of Sepkoski[21] (**a, b**), Alroy[22] (**c, d**) and Zaffos et al[23] (**e, f**), respectively. The mass extinctions marked in bold represent those disabled/enabled in each panel.

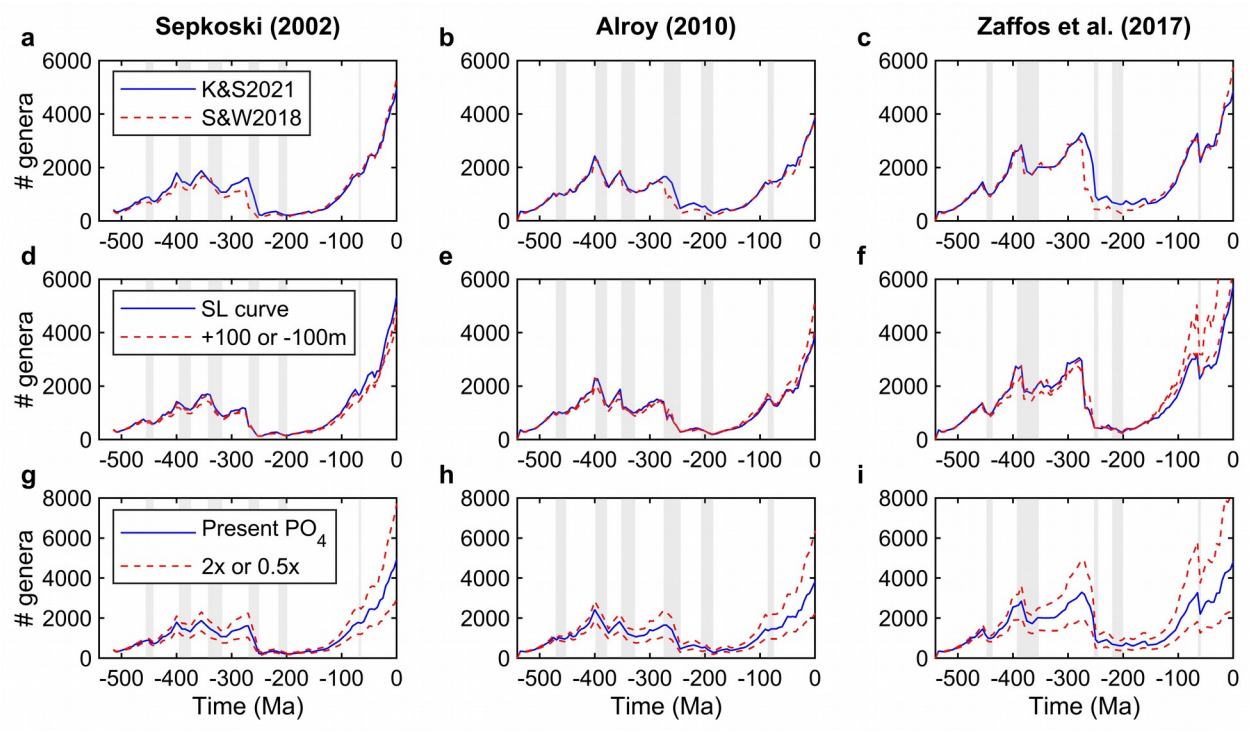

EXTENDED DATA FIGURE 11: Testing the effect of different model configurations and parameter values (sensitivity analyses). a-c, Global diversity dynamics (# genera) reconstructed using the exponential model for two alternative palaeogeographic reconstructions, Kocsis and Scotese[37] (K&S2021) and Scotese and Wright[35] (S&W2018). **d-f**, Effect of changing the sea level +/- 100 m compared to the original paleoDEM grids of Scotese and Wright[35]. **g-i**, Effect of changing the ocean phosphate concentration (x2 and x0.5 with respect to present day concentrations, i.e., default scenario).

EXTENDED DATA TABLE 1. Lin's Concordance Correlation Coefficient (CCC) using different parameter settings in the model.

SEPKOSKI 2002					ALROY 2010					ZAFFOS et al 2017				
Model parameters			Lin's CCC*		Model parameters			Lin's CCC*		Model parameters			Lin's CCC*	
Q10	kfood	ρmax	Exp	Log	Q10	kfood	ρmax	Exp	Log	Q10	kfood	ρmax	Exp	Log
1.5	1	0.035	0.91	0.60	1.5	1	0.035	0.73	0.64	1.5	1	0.035	0.78	0.64
1.5	0.75	0.035	0.91	0.61	1.5	0.75	0.035	0.71	0.66	1.75	1	0.035	0.77	0.60
1.75	1	0.035	0.91	0.55	1.75	1	0.035	0.70	0.60	1.75	0.75	0.035	0.76	0.63
1.75	0.75	0.035	0.91	0.56	1.75	0.75	0.035	0.70	0.62	2	1	0.035	0.75	0.57
2	0.75	0.035	0.91	0.53	2	0.75	0.035	0.70	0.60	2	0.75	0.035	0.75	0.59
2	1	0.035	0.91	0.52	1.5	1	0.04	0.68	0.64	1.5	0.75	0.035	0.75	0.66
2.25	0.75	0.035	0.91	0.51	2	1	0.035	0.68	0.58	2.25	1	0.035	0.74	0.55
2.5	0.75	0.035	0.91	0.49	1.5	0.5	0.035	0.68	0.69	2.25	0.75	0.035	0.74	0.57
2.25	1	0.035	0.90	0.50	1.75	0.5	0.035	0.68	0.65	2.5	1	0.035	0.74	0.53
2.5	1	0.035	0.90	0.49	2	0.5	0.035	0.67	0.62	2.5	0.75	0.035	0.73	0.56
1.5	0.5	0.035	0.90	0.61	2.25	0.75	0.035	0.68	0.60	1.75	0.5	0.035	0.72	0.63
1.75	0.5	0.035	0.90	0.57	2.5	0.75	0.035	0.68	0.59	2.5	0.5	0.035	0.72	0.58
2.5	0.5	0.035	0.90	0.50	2.5	1	0.035	0.68	0.56	2.25	0.5	0.035	0.72	0.59
1.5	1	0.04	0.90	0.59	2	1	0.04	0.67	0.58	1.75	1	0.04	0.72	0.61
2.25	0.5	0.035	0.90	0.52	2.25	1	0.035	0.66	0.57	1.5	1	0.04	0.72	0.65
2	0.5	0.035	0.90	0.54	2.5	1	0.04	0.66	0.56	2	0.5	0.035	0.71	0.61
2	1	0.04	0.89	0.51	1.75	1	0.04	0.66	0.60	2	1	0.04	0.71	0.58
2.5	1	0.04	0.89	0.49	2.5	0.5	0.035	0.65	0.62	2.25	1	0.04	0.70	0.56
1.75	1	0.04	0.89	0.55	2.25	1	0.04	0.65	0.57	2.5	1	0.04	0.70	0.55
2.25	1	0.04	0.89	0.50	2.25	0.5	0.035	0.65	0.61	1.5	0.5	0.035	0.69	0.67
1.5	0.75	0.04	0.88	0.59	1.5	0.75	0.04	0.64	0.66	1.75	0.75	0.04	0.68	0.62
1.75	0.75	0.04	0.88	0.54	1.75	0.75	0.04	0.64	0.62	2.5	0.75	0.04	0.67	0.56
1.75	0.25	0.035	0.88	0.57	2	0.75	0.04	0.63	0.59	2	0.75	0.04	0.67	0.59
1.5	0.25	0.035	0.87	0.60	2	0.25	0.035	0.62	0.65	2.25	0.75	0.04	0.67	0.57
2	0.75	0.04	0.87	0.51	1.75	0.25	0.035	0.62	0.67	2.5	0.25	0.035	0.66	0.60
2.25	0.75	0.04	0.87	0.51	2.5	0.25	0.035	0.62	0.63	1.5	0.75	0.04	0.65	0.67
2	0.25	0.035	0.87	0.54	2.25	0.75	0.04	0.61	0.57	2.25	0.25	0.035	0.65	0.62
2.5	0.75	0.04	0.87	0.50	2.5	0.75	0.04	0.60	0.58	2	0.25	0.035	0.64	0.63
2.5	0.25	0.035	0.87	0.51	2.25	0.25	0.035	0.60	0.65	2.5	0.5	0.04	0.63	0.57
2.25	0.25	0.035	0.87	0.53	1.5	0.25	0.035	0.60	0.69	2.25	0.5	0.04	0.62	0.59
1.5	0.5	0.04	0.86	0.58	1.75	0.5	0.04	0.59	0.65	1.75	0.25	0.035	0.62	0.65
1.75	0.5	0.04	0.85	0.55	2	0.5	0.04	0.59	0.62	2	0.5	0.04	0.62	0.60
2	0.5	0.04	0.85	0.52	1.5	0.5	0.04	0.58	0.68	1.75	0.5	0.04	0.61	0.63
2.5	0.5	0.04	0.84	0.50	2.5	0.5	0.04	0.57	0.60	1.5	0.25	0.035	0.58	0.68
2.25	0.5	0.04	0.84	0.50	2.25	0.5	0.04	0.56	0.60	1.5	0.5	0.04	0.57	0.67
1.5	0.25	0.04	0.83	0.59	2	0.25	0.04	0.52	0.64	2.5	0.25	0.04	0.54	0.59
2.25	0.25	0.04	0.82	0.51	1.5	0.25	0.04	0.51	0.69	2.25	0.25	0.04	0.53	0.60
1.75	0.25	0.04	0.82	0.55	1.75	0.25	0.04	0.51	0.66	2	0.25	0.04	0.51	0.62
2	0.25	0.04	0.82	0.53	2.5	0.25	0.04	0.51	0.62	1.75	0.25	0.04	0.51	0.64
2.5	0.25	0.04	0.81	0.50	2.25	0.25	0.04	0.50	0.63	1.5	0.25	0.04	0.47	0.68

*The CCCs are for the relationship between the normalized diversities estimated from the fossil record and those generated by the exponential (Exp) and the logistic (Log) models. The 15 combinations of model parameters that gave the highest CCC for each mass extinction pattern were selected. Of these, the combination that gave the highest CCC for the relationship between the fossil diversities and the diversities generated by the calibrated logistic (Cal. Log) model was selected as the best (Extended Data Table 1 continued).

1039 **EXTENDED DATA TABLE 1.** (Continued).

SEPKOSKI 2002				ALROY 2010				ZAFFOS et al 2017			
Model parameters			Lin's CCC	Model parameters			Lin's CCC	Model parameters			Lin's CCC
Q10	kfood	ρmax	Cal. Log	Q10	kfood	ρmax	Cal. Log	Q10	kfood	ρmax	Cal. Log
1.5	0.25	0.035	0.95	1.5	0.5	0.035	0.80	1.5	0.75	0.035	0.82
1.5	0.5	0.035	0.95	1.5	0.75	0.035	0.77	1.5	1	0.04	0.81
1.5	0.75	0.04	0.95	**1.75**	**0.5**	**0.035**	**0.77***	**1.75**	**0.5**	**0.035**	**0.81***
2	0.5	0.04	0.94	1.5	1	0.04	0.76	1.5	1	0.035	0.80
2	0.25	0.04	0.94	1.5	1	0.035	0.75	1.75	0.75	0.035	0.79
1.75	**0.5**	**0.035**	**0.94***	1.75	0.75	0.035	0.75	2.25	0.5	0.035	0.79
1.5	0.25	0.04	0.93	2	0.75	0.035	0.73	1.75	1	0.04	0.78
1.5	0.75	0.035	0.93	2.25	0.75	0.035	0.72	1.75	1	0.035	0.78
2.25	0.75	0.04	0.93	1.75	1	0.035	0.72	2	0.75	0.035	0.78
1.75	1	0.04	0.92	2.5	0.75	0.035	0.72	2.5	0.5	0.035	0.78
1.75	0.75	0.035	0.91	2.25	1	0.04	0.71	2.25	0.75	0.035	0.77
1.5	1	0.035	0.90	2	1	0.035	0.71	2	1	0.035	0.76
2	0.75	0.035	0.89	2.5	1	0.04	0.70	2.5	0.75	0.035	0.76
2.25	0.75	0.035	0.88	2.25	1	0.035	0.69	2.25	1	0.035	0.75
2.5	0.75	0.035	0.87	2.5	1	0.035	0.69	2.5	1	0.035	0.74

1040 *The bold numbers show the combination of parameters selected.

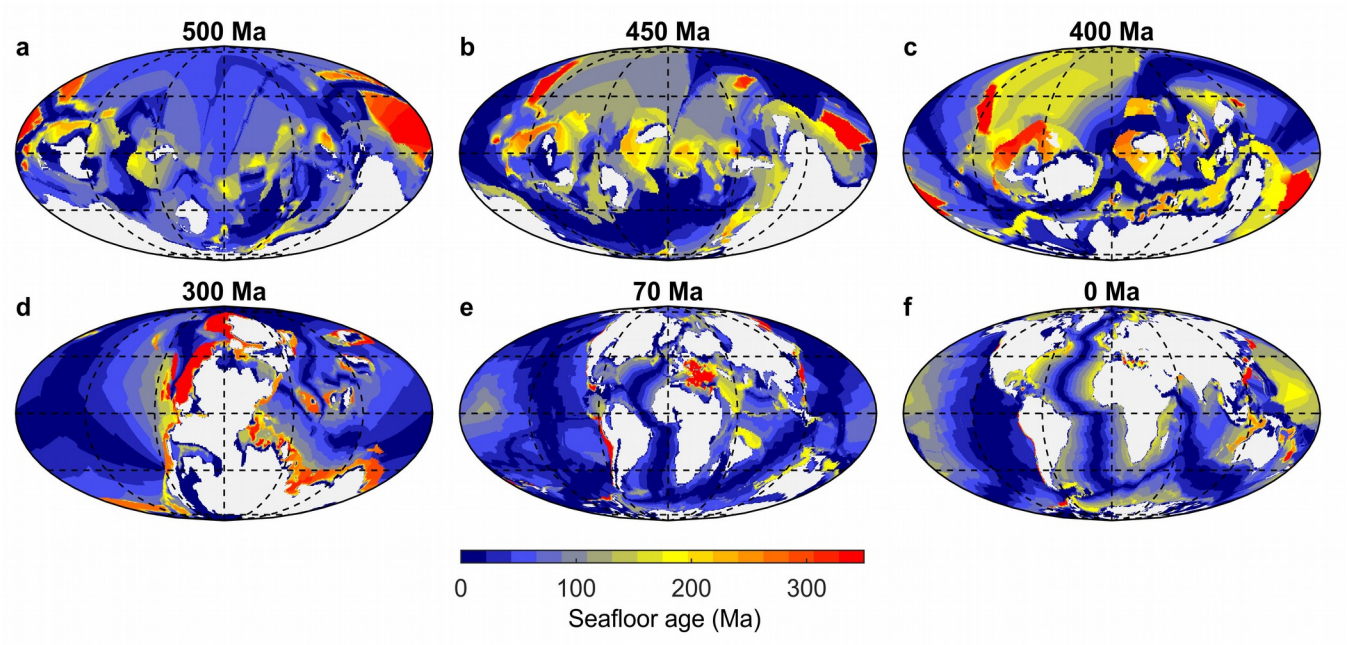

SUPPLEMENTARY FIGURE 1: Model estimates of seafloor age. a-d, Age of the seafloor in open ocean and time that the flooded continental shelves have been underwater in the Cambrian (Guzhangian, 500 Ma), Late Ordovician (Katian, 450 Ma), Early Devonian (Emsian, 400 Ma), Late Carboniferous (Pennsylvanian, 300 Ma), Late Cretaceous (Maastrichtian, 70 Ma) and present (Methods).

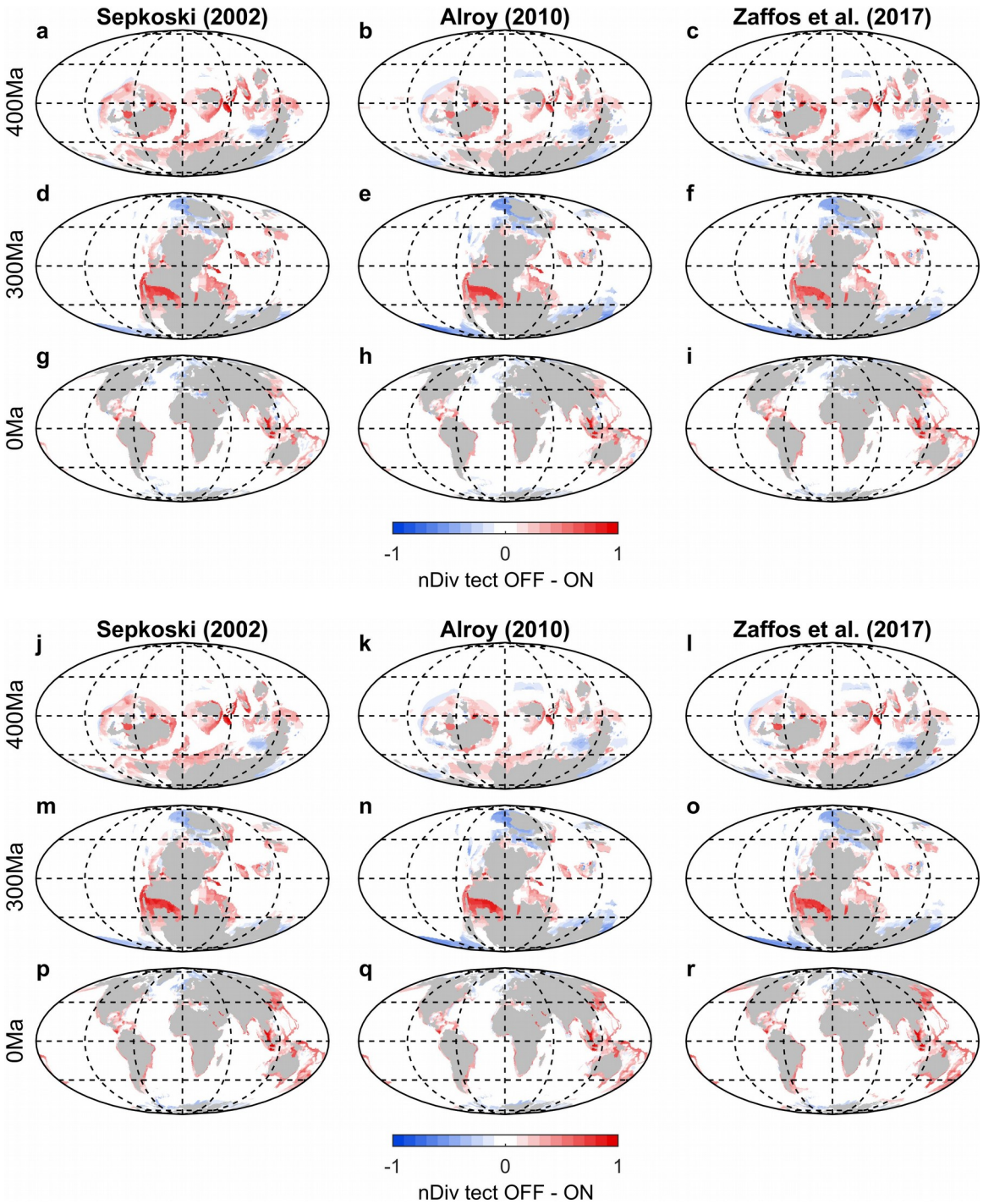

SUPPLEMENTARY FIGURE 2: Testing the impact of plate tectonics on the spatial distributions of diversity. a-i, Comparison of the results of the exponential diversification model without plate tectonics and with plate tectonics. The color code represents the difference between the log-transformed normalized diversities (0-1) produced by the model with static palaeogeography (nDiv tectonics OFF) and the model with variable palaeogeography (nDiv tectonics ON) for three time frames (panels row-wise 400 Ma, 300

Ma and 0 Ma) and three extinction patterns (panels column-wise Sepkoski, Alroy and Zaffos et al). **j-r,** As in panels a-i but for the calibrated logistic model.

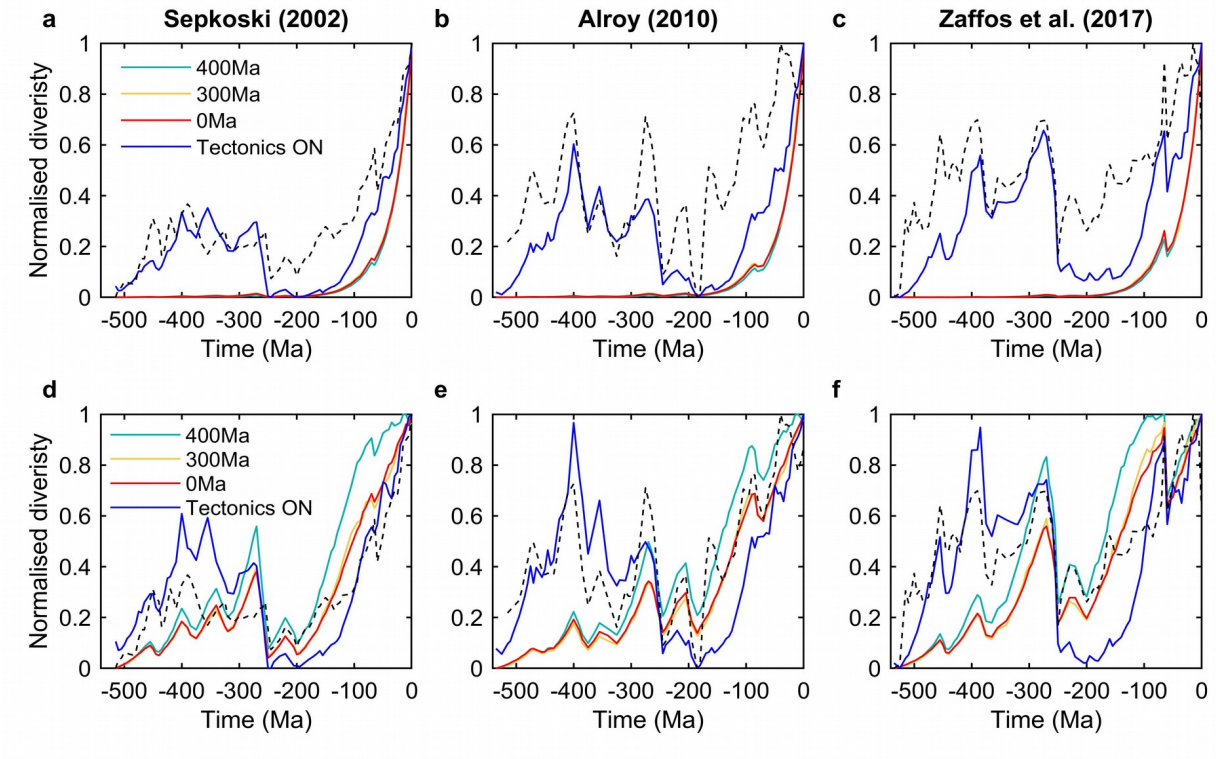

SUPPLEMENTARY FIGURE 3: Testing the impact of plate tectonics on global diversity dynamics. a-c, Global diversity dynamics produced by the exponential diversification model with static palaeogeography (light blue, yellow and red for 400 Ma, 300 Ma and 0 Ma, respectively) and with variable palaeogeography (blue line) for each of the three mass extinction patterns (panels column-wise Sepkoski, Alroy and Zaffos et al). The corresponding fossil diversity curve is superimposed on each panel (grey dashed line). **d-f,** As in panels a-c but for the calibrated logistic model.

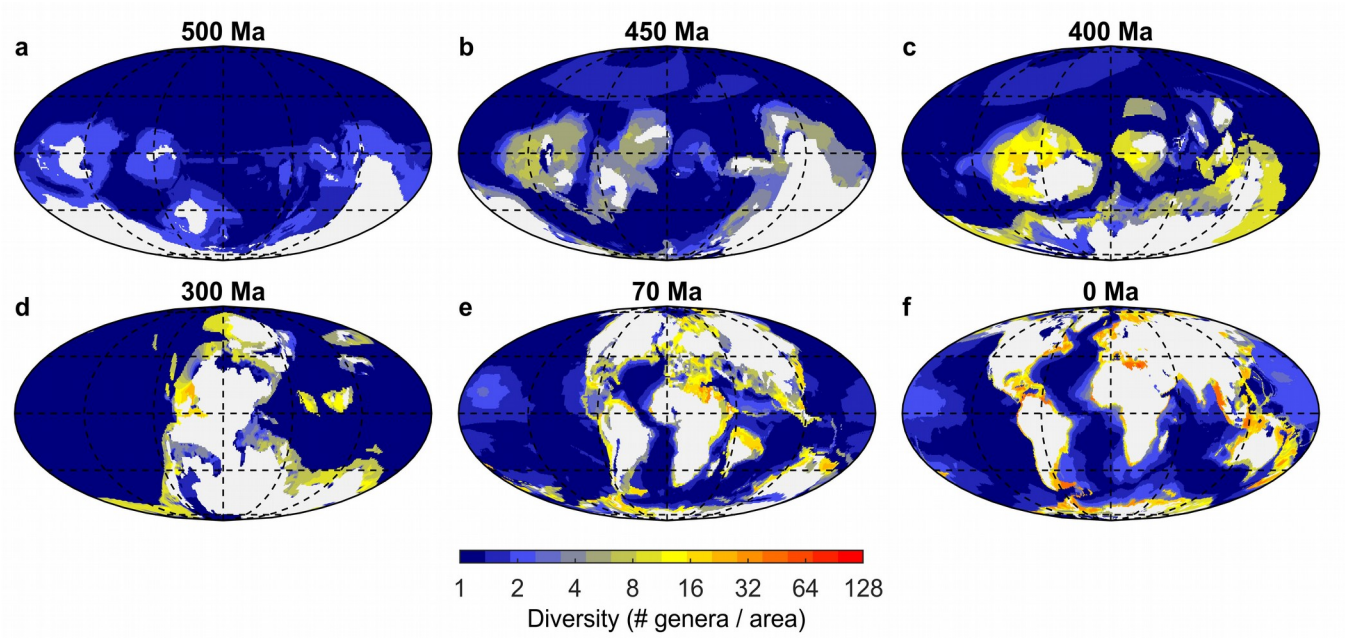

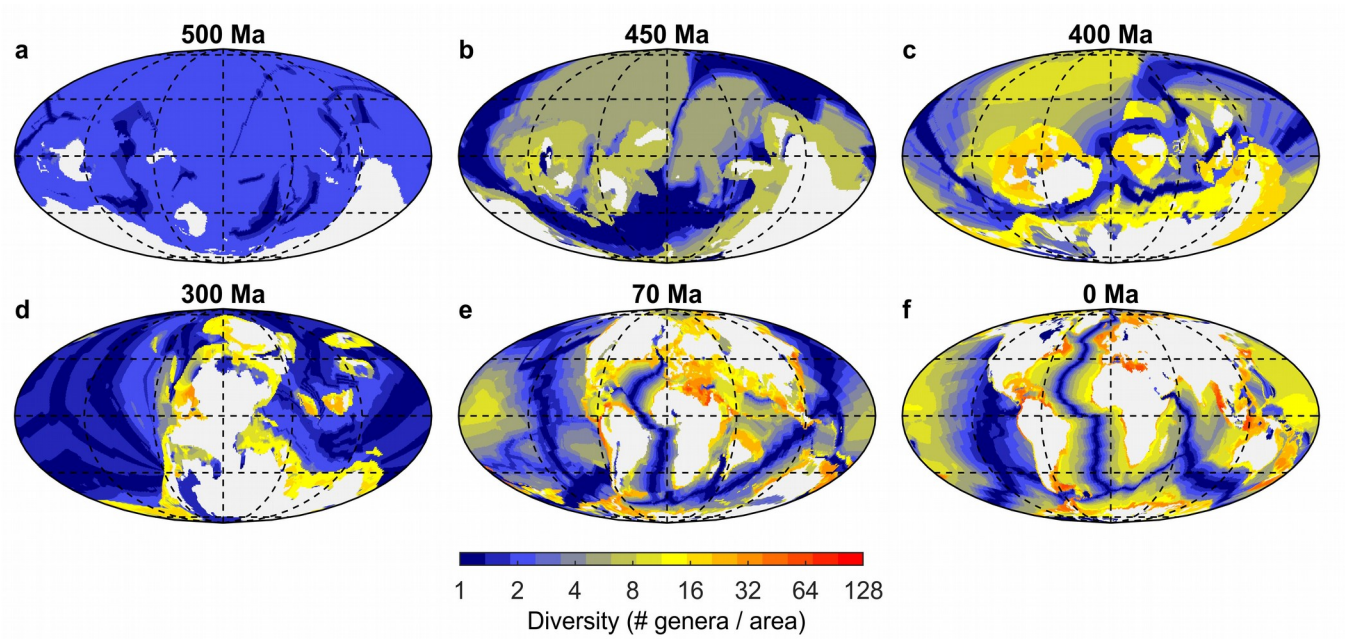

SUPPLEMENTARY FIGURE 4: Testing the effect of disabling the environamnetal forcings. a-f, Spatial distribution of marine animal diversity (# genera / area) in the Cambrian (Guzhangian, 500 Ma), Late Ordovician (Katian, 450 Ma), Early Devonian (Emsian, 400 Ma), Late Carboniferous (Pennsylvanian, 300 Ma), Late Cretaceous (Maastrichtian, 70 Ma) and present generated by the calibrated logistic model after imposing the pattern of mass extinctions extracted from the fossil diversity curve of Sepkoski. This model run uses the following parameters: Q10 = 1 (no temperature dependence), K_{food} = 0.5 molC $m^{-2}y^{-1}$, net

diversification rate limits (ρ_{min} - ρ_{max}) = 0.001-0.035 Myr^{-1} (per capita), and a K_{min} to K_{max} range between 12 and 123 genera. **g-l**, As in panels a-f but disabling both the temperature and food dependence of net diversifciation rate, i.e. Q10 = 1 (no temperature dependence), K_{food} = 0 (no food dependence), net diversification rate limits (ρ_{min} - ρ_{max}) = 0.001-0.035 Myr^{-1} (per capita), and a K_{min} to K_{max} range between 12 and 123 genera.

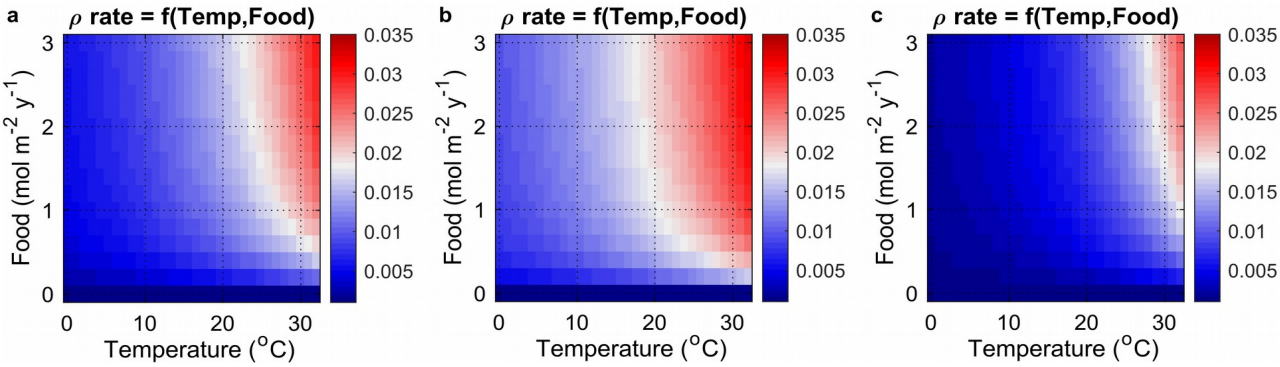

SUPPLEMENTARY FIGURE 5: Interactive effect of seawater temperature and food supply on net diversification rate. **a,** Combined effect of seawater temperature and food supply on net diversification rate (ρ) for the set of parameters used to run the main simulations (i.e. Q_{10} = 1.75; K_{food} = 0.5 molC $m^{-2}y^{-1}$; ρ = 0.001 - 0.035 Myr^{-1}). **b,** Same as upper panel but for two extreme parameter settings (Q_{10} = 1.5; K_{food} = 0.25 molC $m^{-2}y^{-1}$; ρ = 0.001 - 0.035 Myr^{-1}, and **c,** Q_{10} = 2.5; K_{food} = 1 molC $m^{-2}y^{-1}$; ρ = 0.001 - 0.035 Myr^{-1}.

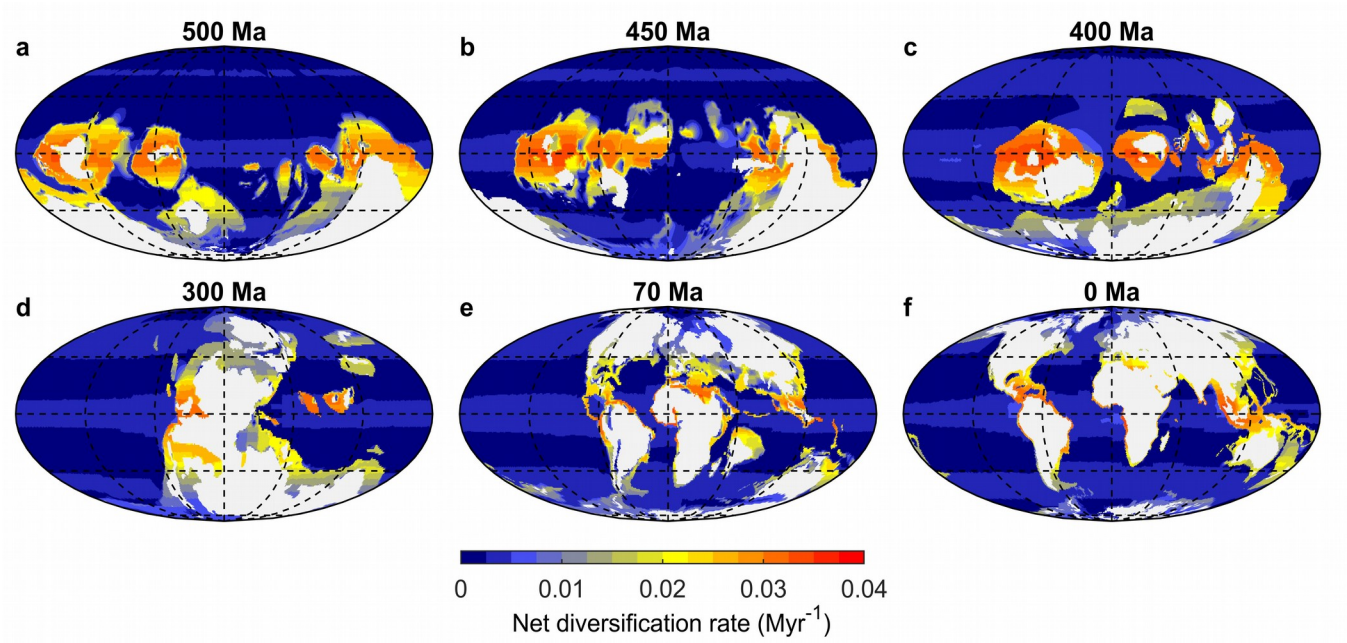

SUPPLEMENTARY FIGURE 6: Model estimates of net diversification rate. a-d, Spatially-resolved net diversification rate in the Cambrian (Guzhangian, 500 Ma), Late Ordovician (Katian, 450 Ma), Early Devonian (Emsian, 400 Ma), Late Carboniferous (Pennsylvanian, 300 Ma), Late Cretaceous (Maastrichtian, 70 Ma) and present.

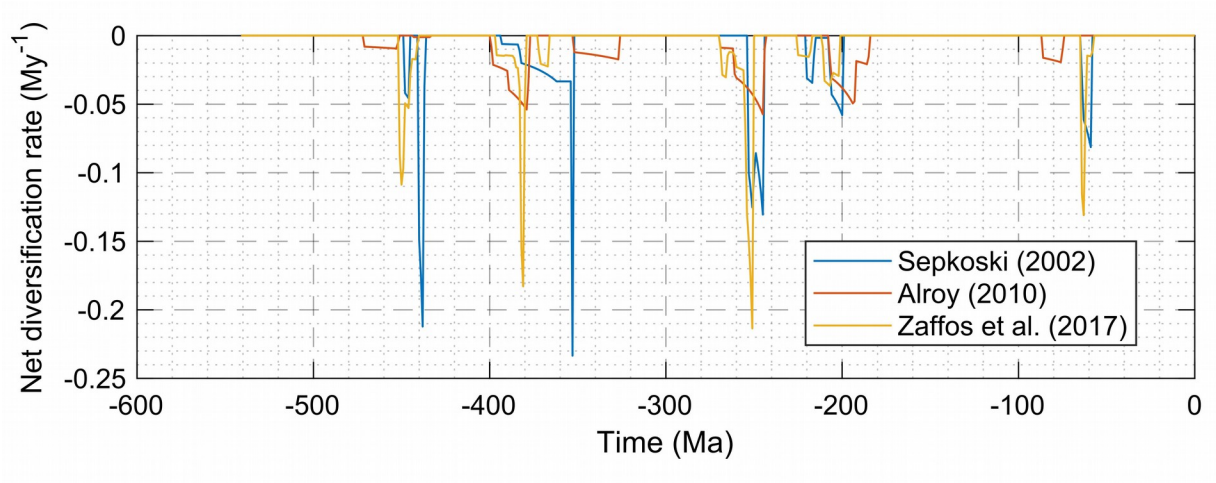

SUPPLEMENTARY FIGURE 7: Mass extinction patterns extracted from the global diversity curves of Sepkoski, Alroy and Zaffos et al. These data are provided as Source Data file 2.

SUPPLEMENTARY TABLE 1. Model parameters and range of parameter values tested.

Symbol	Description	Value	Range tested	units
ρ_{min}	Minimum net diversification rate	0.001	--	Myr^{-1}
ρ_{max}	Maximum net diversification rate	0.035	0.03 – 0.04	Myr^{-1}
Q_{10}	Thermal sensitivity	1.75	1.5 – 2.5	n.u.
K_{food}	Half-saturation constant for food	0.5	0.25 – 1	mol m^{-2} yr^{-1}
lat-lon	Radius of search for immigration	278	0 – 278	Km

SUPPLEMENTARY VIDEOS 1-4. Full Phanerozoic sequences for the spatial reconstructions of diversity based on the saturated logistic model (Supp. Video 1), the exponential model (Supp. Video 2) and the calibrated logistic model (Supp. Video 3). Full Phanerozoic sequences for the spatial reconstructions of diversity-to-carrying capacity ratio (Supp. Video 4). These videos are uploaded along with the manuscript to the journal server. Video format: MP4 (video codec: H264 / AVC)

SOURCE DATA FILE 1. Digitized global diversity curves from original reports.

SOURCE DATA FILE 2. Mass extinction patterns, including the magnitude of diversity loss (represented as negative net diversification rate) as well as the starting time and duration of the mass extinction events imposed in this study as extracted from the fossil diversity curves of Sepkoski, Alroy and Zaffos et al. See also **Supplementary Figure 4** for a graphical representation.

SOURCE DATA FIGURES. The source data for the figures and extended data figures presented in this article are available on GitHub (https://github.com/CarmenGarciaComas/INDITEK). The revised version of the model will be published in ZENODO upon acceptance of the manuscript.

ANNEX 1. Converting Jaccard coefficient to Overlap coefficient

The Jaccard similarity index (J) is the metric most commonly used to express the similarity between two communities. Let us call the intersection of two samples $\alpha_n \cap \alpha_{n+1}$ and their union $\alpha_n \cup \alpha_{n+1}$ The cardinal (number of elements) of a set will be represented by vertical bars, i.e. $\alpha_n = |A_n|$. The Jaccard similarity (J) of α_n and α_{n+1} is then defined as the cardinal of the intersection divided by that of the union:

$$J(A_n, A_{n+1}) = \frac{|A_n \cap A_{n+1}|}{|A_n \cup A_{n+1}|} = \frac{|A_n \cap A_{n+1}|}{|A_n| + |A_{n+1}| - |A_n \cap A_{n+1}|}$$

The J index between points n and n+1 is bounded between 0 and $\min(\alpha_n; \alpha_{n+1})/\max(\alpha_n; \alpha_{n+1})$, where α_n; α_{n+1} are the diversities of two samples. A larger value for J (J > 1) would mean that there are more shared species between the two communities than there are species within the least diverse community, which is ecologically absurd. Yet, using a single similarity decay function can lead the computed value of J to be locally larger than $\min(\alpha_n; \alpha_{n+1})/\max(\alpha_n; \alpha_{n+1})$. To correct this artifact, we used the overlap coefficient (V) instead of J. The overlap coefficient is bounded between 0 and 1, whatever the ratio of diversities. Therefore, using an overlap decay function never creates artifacts.

The overlap coefficient (V), also known as the Szymkiewicz–Simpson coefficient, is defined as the cardinal of the intersection divided by that of the smallest set:

$$V(A_n, A_{n+1}) = \frac{|A_n \cap A_{n+1}|}{(\min(|A_n|, |A_n + 1|))}$$

Without loss of generality, let us consider that α_{n+1} is smaller than α_n. We will call $R = \alpha_n/\alpha_{n+1}$ the ratio of the two cardinals. V can be estimated from J and vice-versa as follows:

$$V(A_n, A_{n+1}) = J(A_n, A_{n+1}) \frac{|A_n| + |A_{n+1}| - |A_n \cap A_{n+1}|}{|A_{n+1}|} = J(A_n, A_{n+1})(1 + R - V(A_n, A_{n+1}))$$

$$J(A_n, A_{n+1}) = \frac{V(A_n, A_{n+1})}{1 + R - V(A_n, A_{n+1})}$$

$$V(A_n, A_{n+1}) = J(A_n, A_{n+1})(1 + R) - J(A_n, A_{n+1}) V(A_n, A_{n+1})$$

$$V(A_n, A_{n+1})(1 + J(A_n, A_{n+1})) = J(A_n, A_{n+1})(1 + R)$$

$$V(A_n, A_{n+1}) = \frac{(1 + R) J(A_n, A_{n+1})}{1 + J(A_n, A_{n+1})}$$

$$V = \frac{\left[1 + \frac{\max(\alpha_n, \alpha_{n+1})}{\min(\alpha_n, \alpha_{n+1})}\right] J}{1 + J}$$